Lyman break and ultraviolet-selected galaxies at $z \sim 1$ – II. PACS 100 μm/160 μm FIR detections[★]

I. Oteo,[1,2]† G. Magdis,[3] Á. Bongiovanni,[1,2,4] A. M. Pérez-García,[1,2,4] J. Cepa,[1,2]
B. Cedrés,[1,2] A. Ederoclite,[5] M. Sánchez-Portal,[4,6] J. A. L. Aguerri,[1,2] E. J. Alfaro,[7]
B. Altieri,[8] P. Andreani,[9,10] T. Aparicio-Villegas,[7,11] H. Aussel,[12] N. Benítez,[7]
S. Berta,[13] T. Broadhurst,[14] J. Cabrera-Caño,[15] F. J. Castander,[16] M. Cerviño,[1,7]
A. Cimatti,[17] D. Cristobal-Hornillos,[5,7] E. Daddi,[18] D. Elbaz,[18]
A. Fernandez-Soto,[19,20] N. Förster Schreiber,[13] R. Genzel,[13]
R. M. Gonzalez-Delgado,[7] C. Husillos,[7] L. Infante,[21] E. Le Floc'h,[18] D. Lutz,[13]
B. Magnelli,[13] R. Maiolino,[22] I. Márquez,[7] V. J. Martínez,[23,24] J. Masegosa,[7]
I. Matute,[7] M. Moles,[5] A. Molino,[7] A. del Olmo,[7] J. Perea,[7] R. Pérez-Martínez,[25]
I. Pintos-Castro,[1,2,26] A. Poglitsch,[13] J. Polednikova,[1,2] P. Popesso,[13] M. Pović,[7]
F. Pozzi,[17] F. Prada,[7] J. M. Quintana,[7] L. Riguccini,[18] E. Sturm,[13] L. Tacconi,[13]
I. Valtchanov[6] and K. Viironen[5]

[1]*Instituto de Astrofísica de Canarias (IAC), E-38200 La Laguna, Tenerife, Spain*
[2]*Departamento de Astrofísica, Universidad de La Laguna (ULL), E-38205 La Laguna, Tenerife, Spain*
[3]*Department of Physics, University of Oxford, Keble Road, Oxford OX1 3RH, UK*
[4]*Asociación ASPID, Apartado de Correos 412, La Laguna, Tenerife, Spain*
[5]*Centro de Estudios de Física del Cosmos de Aragón, Plaza San Juan 1, Planta 2, E-44001 Teruel, Spain*
[6]*Herschel Science Centre (ESAC), Villafranca del Castillo, Spain*
[7]*Instituto de Astrofísica de Andalucía (CSIC), Glorieta de la Astronomía s/n, E-18008 Granada, Spain*
[8]*Herschel Science Centre, European Space Astronomy Centre, Villanueva de la Canada, E-28691 Madrid, Spain*
[9]*ESO, Karl-Schwarzschild-Str 2, D-85748 Garching, Germany*
[10]*INAF Osservatorio Astronomico di Trieste, Via Tiepolo 11, I-34143 Trieste, Italy*
[11]*Observatrio Nacional-MCT, Rua Jos Cristino 77, CEP 20921-400, Rio de Janeiro-RJ, Brazil*
[12]*Laboratoire AIM-Paris-Saclay, CEA/DSM/Irfu – CNRS – Universite Paris Diderot, CE-Saclay, F-91191 Gif-sur-Yvette, France*
[13]*Max-Planck-Institut für extraterrestrische Physik, Postfach 1312, Giessenbachstraße 1, D-85741 Garching, Germany*
[14]*School of Physics and Astronomy, Tel Aviv University, Israel*
[15]*Departamento de Física Atómica, Molecular y Nuclear, Facultad de Física, Universidad de Sevilla, Sevilla, Spain*
[16]*Institut de Ciencies de l'Espai, IEEC-CSIC, Barcelona, Spain*
[17]*Dipartimento di Astronomia, Universit di Bologna, Via Ranzani 1, I-40127 Bologna, Italy*
[18]*Laboratoire AIM, CEA/DSM-CNRS-Universit Paris Diderot, IRFU/Service d Astrophysique, Bt. 709, CEA-Saclay, 91191 Gif-sur-Yvette Cedex, France*
[19]*Instituto de Física de Cantabria (CSIC-UC), E-39005 Santander, Spain*
[20]*Unidad Asociada Observatorio Astronmico (Universitat de València/IFCA-CSIC), Parc Cientfic UV, E-46980 Paterna, Spain*
[21]*Departamento de Astronomía, Ponticia Universidad Catolica, Santiago, Chile*
[22]*Cavendish Laboratory, University of Cambridge, 19 J J Thomson Avenue, Cambridge CB3 0HE, UK*
[23]*Observatori Astronmic de la Universitat de València, Parc Cientfic UV, E-46980 Paterna, Spain*
[24]*Departament d'Astronomia i Astrofsica, Universitat de València, E-46100 Burjassot, Spain*
[25]*XMM/Newton Science Operations Centre (ESAC), Villafranca del Castillo, Spain*
[26]*Centro de Astrobiología, INTA-CSIC, PO Box – Apdo. de correos 78, Villanueva de la Canada Madrid E-28691, Spain*

ABSTRACT

In this work, we report the Photodetector Array Camera and Spectrometer (PACS) 100 μm/160 μm detections of a sample of 42 *GALEX*-selected and far-infrared (FIR)-detected Lyman break galaxies (LBGs) at $z \sim 1$ located in the Cosmic Evolution Survey (COSMOS)

[★] *Herschel* is an ESA space observatory with science instruments provided by European-led Principal Investigator consortia and with important participation from NASA.
† E-mail: ioteo@iac.es

field and analyse their ultraviolet (UV) to FIR properties. The detection of these LBGs in the FIR indicates that they have a dust content high enough so that its emission can be directly detected. According to a spectral energy distribution (SED) fitting with stellar population templates to their UV-to-near-IR observed photometry, PACS-detected LBGs tend to be bigger ($R_{\text{eff}} \sim 4.1$ kpc), more massive [$\log{(M_*/\text{M}_\odot)} \sim 10.7$], dustier [$E_s(B-V) \sim 0.40$], redder in the UV continuum ($\beta \sim -0.60$) and UV-brighter [$\log{(L_{\text{UV}}/\text{L}_\odot)} \sim 10.1$] than PACS-undetected LBGs. PACS-detected LBGs at $z \sim 1$ are mostly disc-like galaxies and are located over the green valley and red sequence of the colour–magnitude diagram of galaxies at their redshift. By using their UV and IR emission, we find that PACS-detected LBGs tend to be less dusty and have slightly higher total star formation rates (SFRs) than other PACS-detected UV-selected galaxies within the same redshift range. As a consequence of the selection effect due to the depth of the FIR observations employed, all our PACS-detected LBGs have total IR luminosities, L_{IR}, higher than 10^{11} L$_\odot$ and thus are luminous IR galaxies. However, none of the PACS-detected LBGs are in the ultra-luminous IR galaxy (ULIRG) regime, $L_{\text{IR}} \geq 10^{12}$ L$_\odot$, where the FIR observations are complete. The finding of ULIRGs-LBGs at higher redshifts ($z \sim 3$) suggests an evolution of the FIR emission of LBGs with cosmic time. In an IRX–β diagram, PACS-detected LBGs at $z \sim 1$ tend to be located around the relation for local starburst similarly to other UV-selected PACS-detected galaxies at the same redshift. Consequently, the dust-correction factors obtained with their UV continuum slope allow us to determine their total SFR, unlike at higher redshifts. However, the dust attenuation derived from UV to NIR SED fitting overestimates the total SFR for most of our PACS-detected LBGs in an age-dependent way: the overestimation factor is higher in younger galaxies. This is likely due to the typical degeneracy between dust attenuation and age in the SED fitting with synthetic templates and highlights the importance of the FIR measurements in the analysis of star-forming galaxies at intermediate redshifts.

1 INTRODUCTION

There are some methods which have been traditionally used to look for star-forming (SF) high-redshift galaxies. Among them, one of the most employed and successful is the Lyman break or dropout technique, which segregates the so-called Lyman break galaxies (LBGs). The technique is based on sampling the Lyman break of galaxies with two broad-band filters close in wavelength, each one located on one side of the break. Since the location in wavelength of the Lyman break depends upon redshift, different combinations of filters pick up galaxies at different redshifts. Many samples of LBGs have been found following that procedure, mainly at $z \gtrsim 3$ by employing optical filters in ground-based telescopes (Madau et al. 1996; Steidel et al. 1996, 1999, 2003; Iwata et al. 2007; Verma et al. 2007; Yabe et al. 2009), but also at $z \sim 2$ (Ly et al. 2009, 2011; Hathi et al. 2010; Basu-Zych et al. 2011; Haberzettl et al. 2012), and at lower redshifts (Burgarella et al. 2006, 2007; Barger, Cowie & Wang 2008; Chen et al. 2013; Oteo et al. 2013a).

In order to accurately study the evolution and the bolometric emission of LBGs, it is essential to have information of the light that is absorbed by dust in the UV and re-emitted in turn in the far-infrared (FIR). With a careful analysis of the UV slope, coupled with appropriate dust attenuation models, Vijh, Witt & Gordon (2003) identify some of the most heavily attenuated specimens in LBGs at $z \sim 2-4$. Furthermore, Finkelstein et al. (2009) find that LBGs at $z \sim 4$ can be detectable with Atacama Large Millimeter/submillimeter Array (ALMA) after a few hours of integration. However, until recently, a few high-redshift LBGs

had been individually detected in FIR (Chapman et al. 2000; Chapman & Casey 2009; Siana et al. 2009; Rigopoulou et al. 2010) and, therefore, a complete and accurate study at different redshifts has not been possible yet. With the advent of the ESA's *Herschel* space observatory (Pilbratt et al. 2010) and its Photodetector Array Camera and Spectrometer (PACS; Poglitsch et al. 2010) and Spectral and Photometric Imaging REceiver (SPIRE; Griffin et al. 2010) instruments, we are in possession of deep FIR data that enable us to study the FIR spectral energy distribution (SED) around the dust emission peak of LBGs as never before. Magdis et al. (2010c) studied for the first time using PACS data the FIR SED of infrared luminous LBGs at $z \sim 3$. Although none of their galaxies are individually detected with *Herschel*, a stacking analysis suggests a median IR luminosity of $L_{\text{IR}} = 1.6 \times 10^{12}$ L$_\odot$. Additionally, complementing their study with multiwavelength data they obtained that for their IR luminosity, MIPS-LBGs are warmer than submillimetre luminous galaxies while they fall in the locus of the $L_{\text{IR}} - T_d$ relation of the local ultra-luminous IR galaxies (ULIRGs). Also with a stacking analysis, Lee et al. (2012) study the FIR emission of LBGs at $3.3 \lesssim z \lesssim 4.3$ obtaining that their IR-to-UV luminosity ratio ($L_{\text{IR}}/L_{\text{UV}}$) is low compared to that observed for $z \sim 2$ LBGs. Furthermore, they obtain that the correlation between the UV continuum slope and the $L_{\text{IR}}/L_{\text{UV}}$ ratio suggests dust properties similar to those of local starbursts (SB) except for the galaxies with the highest luminosities. Davies et al. (2013) employed stacked detections in SPIRE bands of LBGs at $z \sim 3$ to find that a significant fraction of the star formation in these systems is obscured and that the extinction-corrected star formation rate (SFR) does not exhibit

the large values that would be predicted by their UV continuum slope. The latter indicates that the method of assuming an intrinsic UV slope and correcting for dust attenuation may be invalid for this sample and that these are not in fact the most actively SF systems. Burgarella et al. (2011) report the first SPIRE 250 μm and SPIRE 350 μm FIR detections of LBGs by employing data from the Herschel Multi-tiered Extragalactic Survey (HerMES) project (Oliver et al. 2010). They find SPIRE detections for 12 LBGs at $0.7 \lesssim z \lesssim 1.6$ and one at $z \sim 2.0$. All these galaxies are high-mass, luminous IR galaxies (LIRGs), and have redder NUV$-U$ and $U-R$ colours than other SPIRE-undetected galaxies. Oteo et al. (2013b) find 16 LBGs at $z \sim 3$ which are individually detected in PACS under the depth of the observations carried out in the frame of the GOODS-*Herschel* survey (Elbaz et al. 2011). They found that PACS-detected LBGs at $z \sim 3$ are ULIRGs or hyper-luminous IR galaxies and that the dust attenuation factor obtained from the SED-derived dust attenuation with Bruzual & Charlot (2003) templates or from the UV continuum slope cannot reproduce the total SFR of these galaxies.

In this study, we continue the work started in Oteo et al. (2013a) about the physical properties of LBGs and other UV-selected galaxies at $0.8 \le z \le 1.2$ in the Cosmic Evolution Survey (COSMOS; Scoville et al. 2007) field. In that work, we analyse the stellar populations of a sample of *GALEX*-selected LBGs by combining UV *GALEX* measurements and the optical-to-near-IR data coming from the Advanced Large, Homogeneous Area Medium Band Redshift Astronomical (ALHAMBRA) survey (Moles et al. 2008). This combination provides an excellent photometric coverage of the UV-to-near-IR SED of those galaxies. As result, it was found that LBGs at $z \sim 1$ are mostly young galaxies, with a median age of 341 Myr, and have intermediate dust attenuation, $E_s(B - V) \sim 0.2$. Due to their selection criteria they are UV-bright galaxies and have high SFRs. The median value of the stellar mass of the LBGs in the sample is $\log M_*/\mathrm{M}_\odot = 9.74$. Now, we enlarge the photometric coverage of the SEDs of those galaxies by employing IRAC 5.8 μm, IRAC 8.0 μm, MIPS 24 μm and PACS 100 μm/PACS 160 μm data. Actually, one of the advantages of dealing with galaxies at $z \sim 1$ is that their typical observed FIR fluxes make a significant number of objects detectable under the depth of PACS observations used in this work (see Section 2). This allows us to carry out the study of their physical properties avoiding the uncertainties of the optical-based methods that do not take into account the dust emission in the FIR, like the SED fitting with Bruzual & Charlot (2003) templates. The combination of *GALEX*, ALHAMBRA, IRAC, MIPS and PACS data provides a photometric coverage of the SEDs of galaxies which has not been reached with previous data sets. The paper is structured as follows: in Section 2 we define the selection criteria employed to look for our SF galaxies at $z \sim 1$, explain how their SEDs were fitted with synthetic templates and report their FIR counterparts. In Section 3, we study the dust attenuation of our PACS-detected galaxies as a function of the rest-frame UV, total IR, and bolometric luminosity and UV continuum slope. Section 4 shows the study of the SFR and the dust-correction factors. We analyse the relation between the stellar mass and the total and specific SFR (sSFR) in Section 5. The location of our PACS-detected galaxies in a colour–magnitude diagram (CMD) is presented in Section 6, and their morphology is examined in Section 7. The radio emission of our SF galaxies at $z \sim 1$ is shown in Section 8. Finally, we summarize the main conclusions of the work in Section 9.

Throughout this paper, we assume a flat universe with $(\Omega_\mathrm{m}, \Omega_\Lambda, h_0) = (0.3, 0.7, 0.7)$, and all magnitudes are listed in the AB system (Oke & Gunn 1983).

2 UV-SELECTED GALAXIES AND THEIR FIR DETECTIONS

In Oteo et al. (2013a), we selected those LBGs whose Lyman break is located between the *GALEX* FUV and NUV filters, which are centred at the effective wavelengths of 1528 and 2271 Å and have bandwidths of 1344–1786 and 1771–2831 Å, respectively. The LBGs were selected by imposing the colour criterion

$$\mathrm{FUV} - \mathrm{NUV} > 1.5. \tag{1}$$

Additionally, and in order to rule out as much interlopers as possible, we limit the photometric redshift range of the sources to $0.8 \le z \le 1.2$. It should be noted that the combination of *GALEX* and ALHAMBRA data provides accurate photometric redshifts at $z \sim 1$ (Oteo et al. 2013a).

Those galaxies that are undetected in the FUV channel due to the presence of a strong Lyman break were also included in the sample. FUV observations in the COSMOS field have a limiting magnitude of FUV ~ 27 mag (Oteo et al. 2013a). Then, galaxies brighter than that value in the wavelength range covered by the FUV filters should be detected. Since we select galaxies with an FUV $-$ NUV colour cut of 1.5, that limiting magnitude would imply a limit of 25.5 mag in the NUV channel. To be conservative, we choose a limit in the NUV channel of 25 mag and include in the previous sample of LBGs those galaxies that are brighter than 25 mag in the NUV channel, are at $0.8 \le z \le 1.2$ and are undetected in the FUV channel. The non-detection in the FUV channel under those restrictions is likely due to a strong Lyman break. AGN contamination was ruled out by discarding galaxies with X-ray detections (Elvis et al. 2009; Salvato et al. 2011). In total, 1225 *GALEX*-selected LBGs are segregated, with a median redshift of 0.93.

The photometric redshift and other properties such as age, dust attenuation, stellar mass or UV continuum slope were derived by fitting (Bruzual & Charlot 2003, hereafter BC03) templates to their observed *GALEX*+ALHAMBRA fluxes. These templates were built by assuming a Salpeter (1955) initial mass function distributing stars from 0.1 to 100 M$_\odot$, a fixed value of the metallicity ($Z = 0.2\,Z_\odot$) and a time-independent star formation history (SFH). We considered a fixed value of metallicity (see also González et al. 2011; Stark et al. 2013) because it is a parameter difficult to constrain with an SED-fitting procedure (see for example de Barros, Schaerer & Stark 2012; Oteo et al. 2012a). Actually, by running the Zurich Extragalactic Bayesian Redshift Analyzer (ZEBRA) with BC03 templates associated with different metallicities, we obtained in Oteo et al. (2013a) very similar values of the χ_r^2 for individual galaxies, preventing us from constraining the metallicity of our galaxies. The changes in the SED-derived parameters associated with fits with different metallicities are not strongly significant, but they are within their typical uncertainties. The choice of the constant SFR is justified for the comparison with the results obtained with the Kennicutt (1998) calibrations. Therefore, the SED-derived parameters with BC03 templates presented in this work should be understood as those obtained with the previous assumptions for metallicity and SFH. We considered values of age from 1 Myr to 7 Gyr, in steps of 10 Myr from 1 Myr to 1 Gyr and in steps of 100 Myr from 1 Gyr to 7 Gyr. Dust attenuation is included in the templates via the Calzetti et al. (2000) law and parametrized through the colour excess in the stellar continuum, $E_s(B - V)$, for which we select values ranging from 0 to 0.7 in steps of 0.05. We also include intergalactic medium absorption adopting the prescription of Madau (1995). The fits are carried out by using the ZEBRA (Feldmann et al. 2006) code which, in its maximum-likelihood mode, employs a χ^2 minimization

algorithm over the templates to find the one which fits the observed SED of each input object best. We have not included the contribution of emission lines in the SED fits (Zackrisson, Bergvall & Leitet 2008; Schaerer & de Barros 2009, 2010; Atek et al. 2011; Schaerer, de Barros & Stark 2011; de Barros et al. 2012; Schaerer, de Barros & Sklias 2013) since we will deal with dusty FIR-detected galaxies and, according to de Barros et al. (2012), the contribution of emission lines in their SED-derived parameters is not expected to be significant. Each fitted template has a characteristic value of the χ^2. We define the reduced χ^2, χ_r^2, as the ratio between the χ^2 associated with each fitted template and the numbers of filters minus one employed in the SED-fitting procedure, $\chi_r^2 = \chi^2/(N-1)$ (see for example de Barros et al. 2012). Only galaxies with $\chi_r^2 < 10$ were included in the sample. The uncertainties in the SED-derived parameters were derived as the difference between the best-fitted value and its corresponding weighted average, defined as $WA = \sum_i^N P_i f_i/N$, where P_i is the probability that a given template, i, can represent the observed SED of a given galaxy, f_i is the value of one of the physical properties associated with the ith template and N is the number of templates (see Oteo et al. 2013a for more details). In the case of the UV continuum slope, the uncertainties considered here are those rising from the fit of the UV continuum to the exponential law.

In Oteo et al. (2013a), we obtained that the photometric redshifts derived with the combination of *GALEX* and ALHAMBRA data are very accurate, $\sigma_z = (|z_{phot} - z_{spec}|)/(1 + z_{spec}) < 0.05$, for most of our galaxies. As in Oteo et al. (2013a), we adopt the spectroscopic redshifts for those galaxies with available optical spectroscopy in the zCOSMOS survey (Lilly et al. 2007) to redo the SED fits. For those galaxies without zCOSMOS counterpart, we employ the photometric redshift and their associated SED-fitting results. Once each SED is fitted with a BC03 template, the UV continuum slope is obtained for each galaxy directly from its best-fitted template by fitting a power law of the form $f_\lambda \sim \lambda^\beta$ (Calzetti, Kinney & Storchi-Bergmann 1994) to their UV continuum. In this process, we employ the photometric points corresponding to the rest-frame wavelength range $1300 \lesssim \lambda \lesssim 3000$ Å. This approach has the advantage of using all the available fluxes of each source, resulting in higher SNR determinations. The rest-frame UV luminosity, defined in a νL_ν way, for each source is obtained from its best-fitted template shifted to the rest frame and by convolving it with a top-hat filter, 300 Å width, centred in 1500 Å.

With the aim of placing LBGs in a general scenario of FIR-detected SF galaxies at $0.8 < z < 1.2$, we select photometrically a sample of UV-detected galaxies in the same redshift range as the *GALEX*-selected LBGs: we consider all the galaxies detected in *GALEX* (at least in the NUV band) that have an ALHAMBRA counterpart, are detected in PACS 100 μm or PACS 160 μm, and their photometric redshifts are within $0.8 \leq z \leq 1.2$ It should be pointed out that LBGs are contained in this general sample of UV-selected galaxies. The subsample of UV-selected and PACS-detected galaxies which are not LBGs will be called *UV-faint galaxies*. We emphasize that we consider LBGs and UV-faint galaxies independently because the main goal of this work is to analyse the FIR SED of the intermediate-redshift analogues of the colour-selected high-redshift LBGs.

Due to the selection criteria, the main difference between LBGs and UV-selected galaxies is their rest-frame UV luminosity. The selection of LBGs in the FUV channel or the condition NUV < 25 for those FUV-undetected implies that *GALEX*-selected LBGs are intrinsically brighter in the rest-frame UV. The general sample of UV-selected galaxies contains galaxies fainter in the rest-frame UV

Table 1. Summary of the stacking results for the different bins of rest-frame UV luminosity, stellar mass and age (see the text for more details).

Galaxy	PACS 100 μm	PACS 160 μm	Both PACS bands
LBGs	13	11	18
UV-faint	23	14	28

than the LBGs because their only restriction is the photometric redshift and the detection in the NUV and FIR (regardless of the FUV and NUV magnitude).

The PACS FIR data employed in this work are taken within the framework of the PACS Evolutionary Probe (PEP) *Herschel* guaranteed time key project, optimized for FIR studies of galaxy evolution (Lutz et al. 2011). As part of the PEP project, the COSMOS field was targeted in PACS 100 μm and PACS 160 μm. The PACS fluxes used in this study were extracted by using MIPS 24 μm priors (Le Floc'h et al. 2009; Magnelli et al. 2009). The usage of MIPS 24 μm priors is justified because the 24 μm emission is strongly correlated to the FIR emission and, therefore, the catalogues created will not contain a large excess of sources without FIR counterparts. This substantially avoids deblending FIR sources into several unrealistic counterparts, as it might have occurred if, for example, optical-based catalogue with very high source density had been employed. The catalogues were extracted by using a point spread function (PSF) fitting method. The PSFs were directly derived from the science maps when performing a blind source extraction with the code STARFINDER (Diolaiti et al. 2000a,b) and were cut to a 3 pixel radius to extract the catalogues in order to minimize filtering effects on the wings of bright sources. The aperture corrections were determined by independent observations of very bright objects, such as the asteroid Vesta, by simply accounting for the limited radius in the observed PSFs. More details of the reduction and source extraction can be found in Lutz et al. (2011) and references therein. The limiting 3σ fluxes are 5.0 and 11.0 mJy in the PACS 100 μm and PACS 160 μm bands, respectively.

We look for the possible PACS detections of our UV-selected galaxies by using their optical ALHAMBRA positions as reference and considering a matching radius of 2 arcsec. It should be noted that since we are using PACS catalogues built with MIPS 24 μm priors, the coordinates of the sources detected by PACS are those corresponding to the MIPS 24 μm observations. We find that 42 LBGs and 65 UV-faint galaxies are individually detected either in PACS 100 μm or PACS 160 μm. We call those galaxies which are detected in, at least, one PACS band as PACS-detected galaxies. Table 1 summarizes the detections in each PACS band for each kind of PACS-detected galaxy. By inspecting the ACS *I*-band (*F*814*W*) images of the PACS-detected galaxies (see Section 7), we do not find evidence that the FIR fluxes of our sources are contaminated by close neighbours. In Fig. 1, we show the optical ACS *I*-band cutouts along with the IRAC 3.6 μm and MIPS 24 μm contours of two PACS-detected LBGs. With the aim of studying the possible effect of source confusion and analysing how good are the MIPS-based coordinates (employed as priors) and the optical ones, we represent one of the best favourable (big galaxy with no close companions) and the least favourable cases (where it can be thought that there is source confusion with close neighbours). It can be seen that in the two cases, the MIPS 24 μm emission (and therefore the PACS emission) truly comes from the PACS-detected LBG and, thus, there is no evidence of source confusion. In Oteo et al. (2013a), we found that the SED fitting with ALHAMBRA data in the optical and
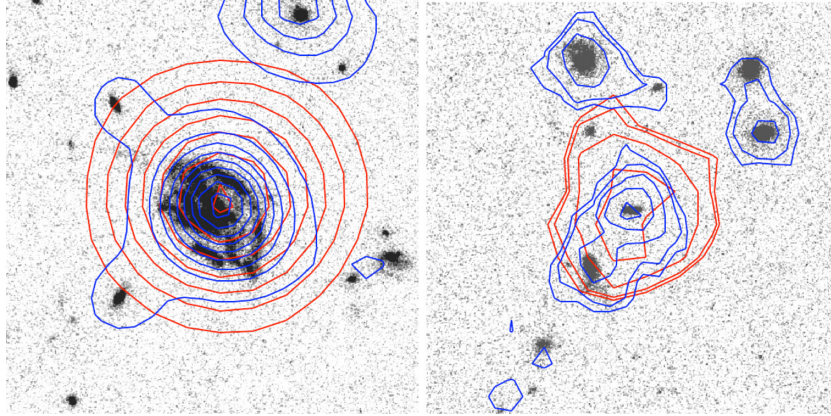
Figure 1. ACS *I*-band images along with the IRAC 3.6 μm (blue) and MIPS 24 μm (red) contours for two PACS-detected LBGs. The PACS-detected LBGs are the galaxies located in the centre of each image. To show how good are MIPS coordinates with respect to optical data, we have selected for the plot one of the best cases and one of the worst cases of FIR identifications. Left: favourable case where the PACS-detected LBG is a big galaxy without close neighbours. Right: unfavourable case where the PACS-detected galaxy is small and it is surrounded by some close neighbours. In the two cases, it is clear that the MIPS 24 μm emission (and therefore the PACS emission) truly comes from the PACS-detected LBG.
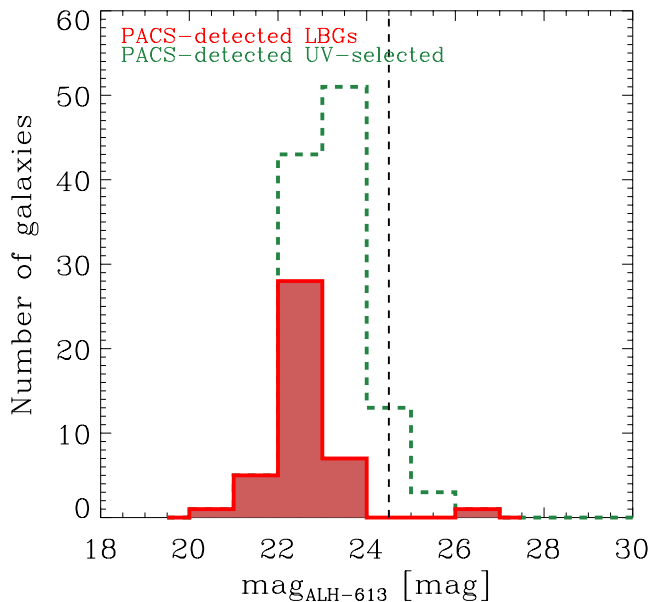
Figure 2. Distribution of the ALH-613 band magnitude for our PACS-detected LBGs (red filled histogram) and PACS-detected UV-selected galaxies (green dashed histogram). The vertical dashed line represents a magnitude of 24.5 mag and indicates the approximate minimum brightness limit down to which the SED fitting in the UV, optical and near-IR with ALHAMBRA data can be considered reliable.

near-IR could be considered reliable only for galaxies brighter than 24.5 mag in the ALH-613 band. Fainter galaxies in the optical have low values of χ_r^2 likely due to high photometric uncertainties rather than to truly good fitting. In Fig. 2, we represent the optical ALH-613 magnitude of our PACS-detected galaxies. It can be seen that most of the galaxies are brighter than the previous value and, therefore, the values of χ_r^2 are likely due to a good SED fitting rather than high photometric uncertainties. Additionally, Fig. 2 indicates that PACS-detected LBGs are typically brighter ($m_{\mathrm{ALH-613}} \sim 22.4$) than UV-faint galaxies ($m_{\mathrm{ALH-613}} \sim 23.2$). This is a direct consequence of their selection criteria. Furthermore, PACS-detected LBGs are among the optical brightest galaxies in the whole sample of *GALEX*-selected LBGs presented in Oteo et al. (2013a).

Summarizing, we define the samples of PACS-detected LBGs, UV-selected and UV-faint galaxies as

$$\{\text{LBGs :}\} = \{\text{GALEX} + \text{ALHAMBRA} :$$
$$\text{(i)} \quad \text{FUV} - \text{NUV} > 1.5 \quad \text{or}$$
$$\text{NUV} < 25 \quad \text{and} \quad \text{FUV} - \text{undetected}$$
$$\text{(ii)} \quad 0.8 < z < 1.2$$
$$\text{(iii)} \quad \text{non} - \text{AGNs}$$
$$\text{(iv)} \quad \text{PACS} - \text{detected}\}$$

$$\{\text{UV} - \text{selected :}\} = \{\text{GALEX} + \text{ALHAMBRA} :$$
$$\text{(i)} \quad \text{NUV-detected with no restriction on FUV}$$
$$\text{(ii)} \quad 0.8 < z < 1.2$$
$$\text{(iii)} \quad \text{non} - \text{AGNs}$$
$$\text{(iv)} \quad \text{PACS} - \text{detected}\}$$

$$\{\text{UV-faint}\} = \{\text{UV-selected}\} - \{\text{LBGs}\}.$$

Fig. 4 shows the UV-to-FIR SED of nine PACS-detected LBGs that represent the typical SED-fitting results for our galaxies. It can be seen that the combination of *GALEX*, ALHAMBRA, IRAC, MIPS and PACS data provides an excellent photometric coverage of the SEDs of the studied galaxies.

Mid- and far-IR detection rates of UV-selected galaxies vary with basic properties of the galaxies. Because of the larger detection rate in the mid-IR compared to the far-IR we discuss mid-IR detection rates, but trends in the FIR are consistent. Fig. 3 gives the detection rate in MIPS 24 μm of the whole sample of UV-selected galaxies at $0.8 < z < 1.2$ built in Oteo et al. (2013a), as a function of their SED-derived rest-frame UV luminosity, UV continuum slope, age, dust attenuation and stellar mass. MIPS 24 μm detections were searched by using a matching radius of 2 arcsec and using the data coming from the S-COSMOS survey (Sanders et al. 2007).

First, it can be seen that the detection rate in MIPS 24 μm increases with the rest-frame UV luminosity, i.e. UV-bright galaxies are more likely detected in the FIR. This trend has been also reported in other works which analyse the IR properties of
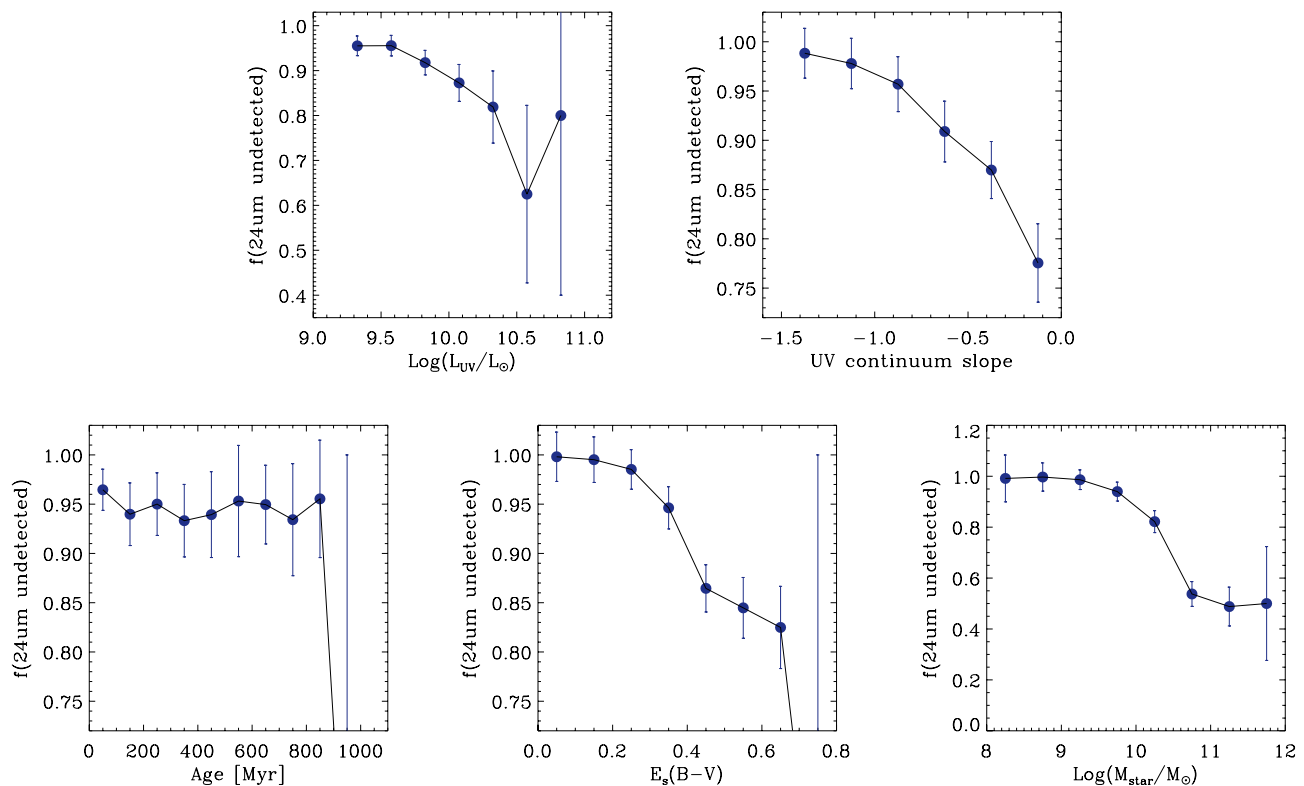
Figure 3. Undetected fraction in MIPS 24 μm of the whole population of PACS-detected LBGs and UV-faint galaxies at $z \sim 1$ as a function of their rest-frame UV luminosity, UV continuum slope, age, dust attenuation and stellar mass. The error bars have been obtained assuming Poisson statistic. The wider error bars in the points associated with the UV-brightest, oldest, dustiest and most massive galaxies are due to a low number of galaxies in those specific bins.

UV-selected galaxies at lower (see for example Oteo et al. 2012b) and higher redshifts (see for example Reddy et al. 2010). Furthermore, the SPIRE-detected LBGs reported in Burgarella et al. (2011) are UV-bright galaxies, with an average value of $\log \langle L_{\mathrm{UV}}/L_{\odot} \rangle = 10.7$, most of them being UV-luminous galaxies. Other clear tendencies between the detection rate in the FIR and the SED-derived physical properties of galaxies are those related to the UV continuum slope, dust attenuation and stellar mass. Fig. 3 indicates that galaxies which have redder UV continuum and are dustier and more massive are more likely detected in the FIR. We do not find any significant relation between the MIPS 24 μm detection rate and the age of the galaxies.

2.1 Rest-frame UV, IR and bolometric luminosities

As indicated before, the rest-frame UV luminosities, L_{UV}, for the galaxies studied in this work are obtained from the BC03 templates which fit the observed UV-to-near-IR SED of each galaxy best by shifting them to the rest-frame and convolving them with a top-hat filter centred in 1500 Å with 100 Å width. Throughout this study, we consider that the rest-frame UV luminosities indicated as L_{UV} are expressed in νL_{ν} units, whereas the rest-frame UV luminosities indicated as L_{1500} are expressed in L_{ν} units. With the aim of obtaining the total IR luminosities, $L_{\mathrm{IR}}[8-1000\,\mu\mathrm{m}]$, of our PACS-detected galaxies, we carry out SED fits with ZEBRA to their observed IRAC 8.0 μm, MIPS 24 μm and PACS 100 μm/PACS 160 μm fluxes with (Chary & Elbaz 2001, hereafter CE01) templates. Once the best templates are found, they are shifted to the rest-frame and then integrated between 8 and 1000 μm to obtain L_{IR}. In this way we avoid applying the relation between L_{IR} and SED shape, known

to fail at high redshift (Elbaz et al. 2010, 2011). We have computed the uncertainties in the total IR luminosities by modifying the IRAC/MIPS/PACS fluxes randomly within their uncertainties and obtaining the new L_{IR} with the same procedure above. We repeat this 1000 times and find that the typical deviations in $\log (L_{\mathrm{IR}}/L_{\odot})$ are within 0.1 dex. For comparison, we also fit the FIR SED of our PACS-detected galaxies (in the same bands) with (Dale & Helou 2002, hereafter DH02) templates. The typical uncertainties for the total IR luminosity obtained with DH02 templates are obtained in the same way as for those obtained with CE01 templates and have also a value of $\log (L_{\mathrm{IR}}/L_{\odot}) = 0.1$ dex. The upper panel of Fig. 5 shows the relation between the total IR luminosities derived with CE01 and DH02 templates. It can be seen that DH02 templates tend to give higher values for our PACS-detected galaxies, although many of the points are within the uncertainties. In Fig. 4, nine examples of IR SED fittings can be found (red curves).

In the bottom panels of Fig. 5, we compare the total IR luminosities derived with PACS (with both CE01 and DH02 templates) data with those obtained from single-band extrapolations with MIPS 24 μm data only (see Elbaz et al. 2010). It can be seen that MIPS 24 μm alone tends to slightly overestimate the total IR luminosities of our PACS-detected sources in only 0.1 dex typically when employing CE01 templates. For DH02 templates, the points are nearer the one-to-one relation. For both kinds of FIR templates and for most of the galaxies, the deviations are lower than 0.2 dex. Therefore, there is good agreement between those quantities within the uncertainties of the total IR luminosities. This is only true for FIR-bright galaxies with PACS detections, but it does not have to be true for FIR-fainter sources detected in MIPS 24 μm and PACS-undetected. There is no reason to choose between one of the two
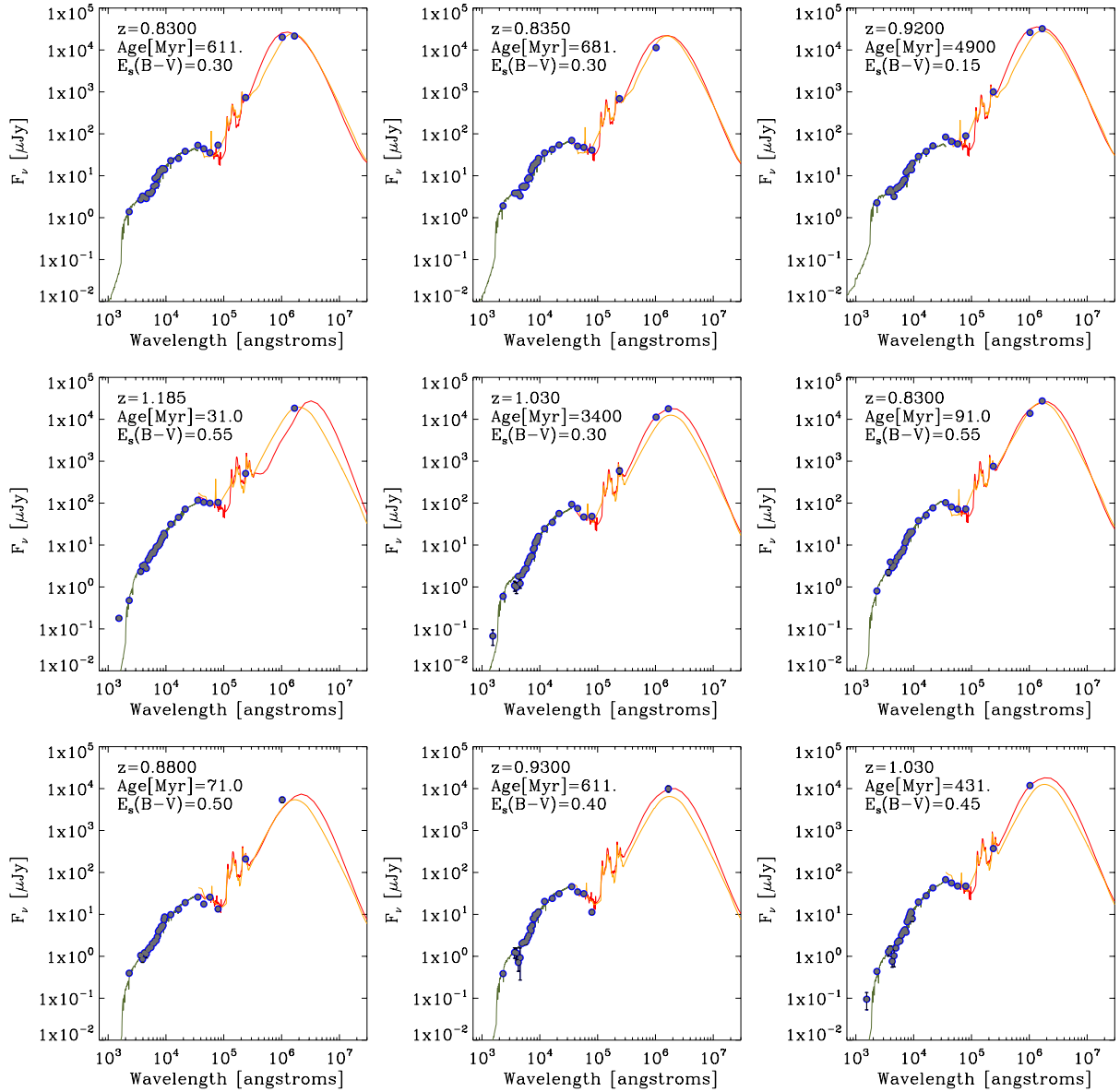
Figure 4. Rest-frame UV-to-FIR SED of nine randomly selected PACS-detected LBGs. These examples are representative of the SED-fitting results for our whole sample of our PACS-detected galaxies. The grey points denote the observed UV-to-FIR fluxes of the galaxies. The green curves represent the best-fitted BC03 templates to the UV-to-IRAC 4.5 μm fluxes of each galaxy. The BC03 templates considered in the representations and fits are associated with time-independent SFH and a fixed metallicity of $Z = 0.2\,Z_{\odot}$ (see Oteo et al. 2013a for more details). SED-derived redshift, age and dust attenuation associated with the represented BC03 templates are also indicated. The orange and red curves denote the best-fitted CE01 and DH02 templates, respectively, to the IRAC 5.8 μm to PACS fluxes of each galaxy.

sets of FIR templates. It should be remarked that the fact that the points are located closer to the one-to-one relation when using DH02 templates does not mean that these templates provide better determinations of the total IR luminosity since the MIPS 24 μm single-band extrapolations do not have to apply for our galaxies. From now on, we decide to report the results obtained with CE01 templates.

Finally, we define the bolometric luminosity, L_{bol}, of our galaxies as the sum of the UV and IR luminosities: $L_{bol} = L_{UV} + L_{IR}$ (see for example Reddy et al. 2006).

Fig. 6 shows the distribution of L_{UV}, L_{IR} and L_{bol} for our PACS-detected galaxies. As expected from their selection criteria and supported by the results of a Kolmogórov-Smirnov (K-S) test, LBGs tend to be UV-brighter than UV-faint galaxies. However, despite

their difference in the UV selection criteria, the L_{IR} span within a similar range. Their total IR luminosities place PACS-detected LBGs and UV-faint galaxies in the LIRG regime, i.e. they have $10^{11} < L_{IR}/L_{\odot} < 10^{12}$. The median values of L_{IR} for PACS-detected LBGs and UV-faint galaxies are $\log{(L_{IR}/L_{\odot})} = 11.7$ and 11.6, respectively. It should be noted that the fact that all our PACS-detected galaxies have $L_{IR} > 10^{11}\,L_{\odot}$ is a consequence of the depths of the PACS observations in the COSMOS field, since they are not deep enough to recover galaxies with $L_{IR} < 10^{11}\,L_{\odot}$. However, we do not find any PACS-detected LBG at $0.8 \lesssim z \lesssim 1.2$ in the ULIRG regime ($10^{12} < L_{IR}/L_{\odot} < 10^{13}$) or with higher total IR luminosities, where the observations are complete. A population of ULIRG-LBG appear at higher redshifts, suggesting evidence for an evolution of the FIR emission of LBGs (Oteo et al. 2013b). A similar behaviour has
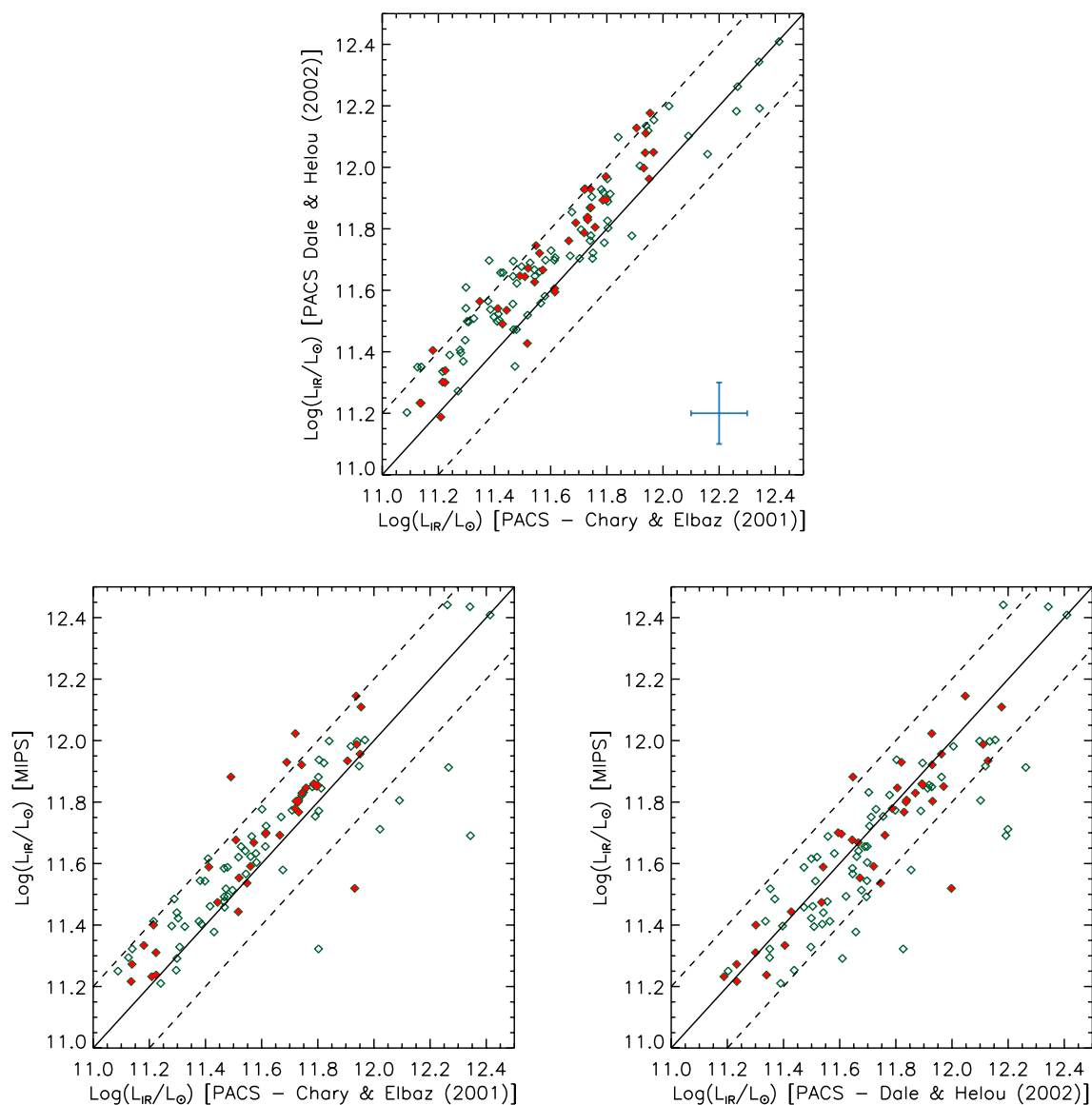
Figure 5. Upper panel: comparison between the total IR luminosity for our PACS-detected LBGs (red dots) and UV-faint galaxies (green diamonds) with CE01 and DH02 templates. The blue bars indicate the typical uncertainties in the determinations of the total IR luminosity. Bottom panels: comparison between the MIPS 24 μm-derived and PACS-derived total IR luminosities for our PACS-detected LBGs (red dots) and UV-faint galaxies (green diamonds) with CE01 (left-hand panel) and DH02 (right-hand panel) templates. Only galaxies with available MIPS and PACS fluxes are included. The MIPS-based L_{IR} are obtained by using single-band extrapolations from the observed MIPS 24 μm to L_{IR} employing the CE01 templates. The PACS-based total IR luminosities are derived by fitting CE01 templates to the observed IRAC 8.0 μm, MIPS 24 μm, PACS 100 μm and PACS 160 μm fluxes of the sources. The straight line indicates where both determinations would agree and the dashed lines indicate deviations of ±0.2 dex around the one-to-one relation.

been suggested for the other classical population of high-redshift SF galaxies: Lyα emitters (Oteo et al. 2011, 2012a,b). The distributions of the bolometric luminosities are similar to the IR ones, since the UV contribution to the bolometric luminosity is low for LIRGs.

2.2 Stacking analysis

Many of our GALEX-selected LBGs are undetected in PACS 100 μm/PACS 160 μm. In order to gain insight about the FIR properties of these PACS-undetected LBGs, we perform a stacking analysis in the PACS 160 μm band. We choose this band for the stacking because it is the closest one to the dust emission peak and, therefore, the determination of the FIR properties will be more accurate than with the PACS 100 μm band. We apply here the traditional stack-

ing procedure previously adopted in some other works based on *Herschel* data (Magdis et al. 2010c; Rodighiero et al. 2010; Reddy et al. 2012). We extract 60 arcsec × 60 arcsec images centred in the optical position of the PACS-undetected galaxies and then these cutouts are combined by using a median algorithm. We use the median image instead of the mean to ensure that the result is not very dependent on the presence of bright outliers. In the stacking we use the cutouts extracted from residual PACS 160 μm images, which are obtained from the science images by removing all the PACS 160 μm detected sources in the catalogue with SNR > 3.

We consider different samples to stack among the whole sample of PACS-undetected LBGs related to their different properties that will be studied in this work in the next sections. In this way, we arbitrarily split our sample of PACS-undetected LBGs into bins of
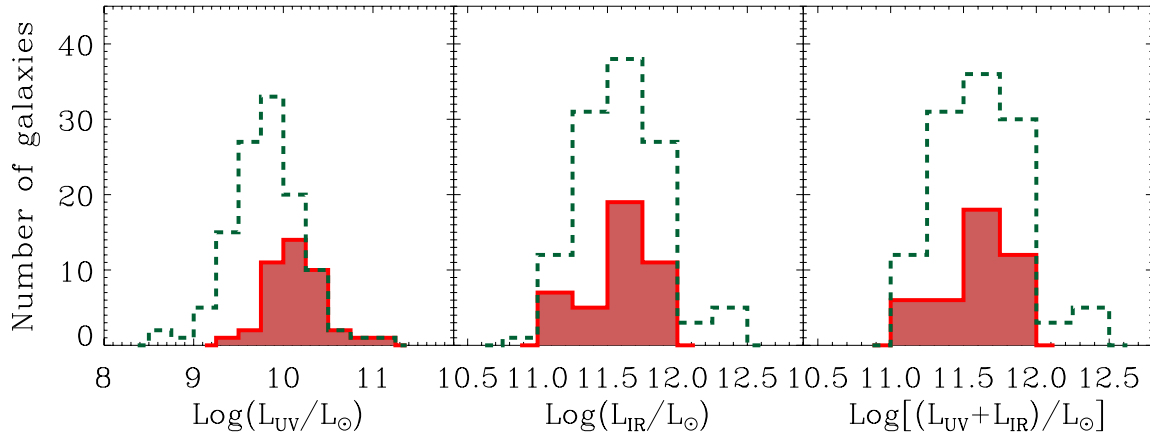
Figure 6. Distribution of the rest-frame UV (left), IR (middle) and bolometric (right) luminosities for our PACS-detected LBGs (red shaded histograms) and the whole sample of LBGs and UV-faint galaxies (green dashed histograms).

Table 2. Summary of the stacking results for the different bins of rest-frame UV luminosity, stellar mass and age considered in this work (see the text for more details).

Bin	N	$f_{160\,\mu m}$ (mJy)
$9.75 \leq \log(L_{UV}/L_\odot) \leq 10.0$	435	0.81 ± 0.21
$10.00 < \log(L_{UV}/L_\odot) \leq 10.25$	338	0.59 ± 0.24
$10.25 < \log(L_{UV}/L_\odot) \leq 10.50$	108	0.78 ± 0.40
$9 \leq \log(M_*/M_\odot) \leq 10.0$	612	0.48 ± 0.13
$10.0 \leq \log(M_*/M_\odot) \leq 11.0$	352	0.98 ± 0.23
Age $< 100\,$Myr	238	0.45 ± 0.27

rest-frame UV luminosities, stellar mass and SED-derived age, as indicated in Table 2. We distinguish only one range of age with the aim of studying if the youngest galaxies in our sample behave differently from the rest of the population. The number of galaxies in each bin is also indicated in Table 2.

In order to measure the uncertainties in the stacked images, we follow a similar procedure as those employed, for example, in Reddy et al. (2012) or Magdis et al. (2010c). We perform stacking in the PACS 160 μm residual map in N random positions, where N is the number of galaxies in each bin of rest-frame UV luminosity, stellar mass and age. We then measure the resultant fluxes in the stacked images and repeat this process 1000 times. It should be noted that the stacking in this case should be done with the residual images since otherwise there would be a high contribution of FIR emission of real PACS-detected sources. The width of the distribution of the stacked fluxes in each bin is considered as the uncertainty in the stacked PACS 160 μm flux in each case. The lower the number of galaxies in each bin, the higher is the uncertainty in the stacked flux. These uncertainties span from $\Delta f_{160\,\mu m} = 0.40$ to 0.13 mJy. The uncertainties in each bin are shown in Table 2. In addition to giving an estimation of the uncertainty of the stacking procedure, this process also provides information about the probability of obtaining significant stacked fluxes when stacking in random positions along the images and, therefore, representing fluxes not related to real sources. If the width of the distribution was as high as the stacked flux obtained in the real optical position of the LBGs, there would be a non-negligible probability of a chance measurement of stacked flux in a position which does not correspond to real sources and, therefore, the stacking procedure would not be reliable. Following this idea, we will consider that we obtain a stack detection if each stacked PACS 160 μm flux is higher than $3 \times \Delta f_{160\,\mu m}$.

As a first step, and in order to study the reliability of the stacking analysis, we perform a stacking in the PACS 160 μm band of all the *GALEX*-selected sources which are detected in MIPS 24 μm but undetected in PACS. At the redshift range of our galaxies, MIPS 24 μm single-band extrapolations to the total IR luminosities give reasonably good results (Elbaz et al. 2010, 2011). Therefore, in this case we can compare the MIPS-derived total IR luminosities with those obtained from the stacked PACS 160 μm flux and study the agreement between the results. The PACS 160 μm stacked flux obtained for the MIPS-detected LBGs with the cutouts taken from the PACS 160 μm residual image is $f_{160\,\mu m} = 2.7 \pm 0.4$ mJy. In order to obtain its associated total IR luminosity, we employ a single-band extrapolation method from the PACS 160 μm flux to the total IR luminosity, obtaining a value of $\log(L_{IR}/L_\odot) = 11.0$. The median value of the MIPS 24 μm flux for the MIPS-detected/PACS-undetected LBGs is $f_{24\,\mu m} = 0.2 \pm 0.1$, where the indicated uncertainty corresponds to the standard deviation of the distribution of the MIPS 24 μm fluxes. Applying again a single-band extrapolation, we obtain that its associated total IR luminosity is $\log(L_{IR}/L_\odot) = 11.3$. This value is slightly higher than that obtained from stacking in PACS 160 μm but still compatible with the typical uncertainties of the single-band extrapolations for obtaining the total IR luminosity and the uncertainties of the MIPS 24 μm and PACS 160 μm fluxes of the stacked sources.

For each of the bins, we applied the stacking procedure outlined above with the PACS 160 residual images. We only find stacked detections in the bin associated with the lowest rest-frame UV luminosity and the bin associated with the highest stellar mass. Fig. 7 shows the stacked PACS 160 μm images in those two ranges where we recover a stacked detection. The stacked fluxes are shown in Table 2. The total IR luminosities associated with the stacked PACS 160 μm fluxes are obtained by using single-band extrapolations (Elbaz et al. 2010). In the following analysis, the values of the rest-frame UV luminosities, stellar mass and age for each bin are represented by the median values for all the galaxies belonging to each one.

2.3 SED-derived properties of PACS-detected galaxies

In Oteo et al. (2013a), we analysed the physical properties of *GALEX*-selected LBGs at $0.8 \lesssim z \lesssim 1.2$ by employing an SED-fitting procedure with BC03 templates. This allowed us to study their rest-frame UV luminosity, UV continuum slope, age, dust
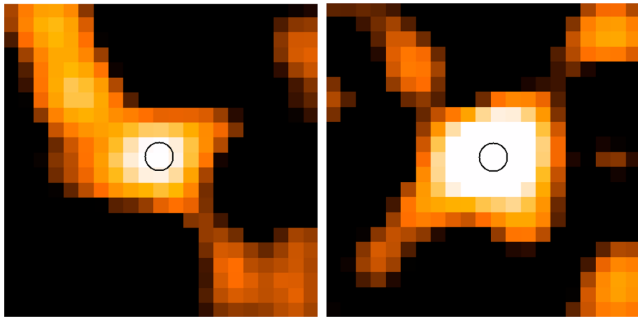
Figure 7. PACS 160 μm stacked images (60 arcsec × 60 arcsec) in the two bins where a stacked detection is recovered (see the text for more details). Left: stacking for galaxies with $9.75 \leq \log(L_{UV}/L_{\odot}) \leq 10.0$. Right: stacking for galaxies with $10.0 \leq \log(M_*/M_{\odot}) \leq 11.0$.

attenuation, dust-corrected total SFR and stellar mass. Furthermore, we have discussed before the trends between the MIPS 24 μm detections and the SED-derived physical properties, finding that the objects more likely detected in the FIR are more massive, dustier, redder and UV-brighter. In this section, we examine the SED-derived physical properties of our PACS-detected LBGs and study the differential properties between PACS-detected and PACS-undetected ones.

Properties of PACS-detected LBGs. We focus first on the SED-derived physical properties of the PACS-detected LBGs (Fig. 8). Their stellar populations have a median age of 341 Myr, rest-frame UV luminosity of $\log(L_{UV}/L_{\odot}) = 10.1$, dust attenuation of $E_s(B-V) = 0.4$, UV continuum slope of $\beta = -0.6$, stellar mass of $\log(M_*/M_{\odot}) = 10.1$ and specific SFR $\log(sSFR[Gyr^{-1}]) = 0.51$. The median value of the stellar mass of our PACS-detected LBGs is slightly lower than that reported in Burgarella et al. (2011) for their SPIRE-detected LBGs. This difference is likely due to their different IR-selection criterion: the selection in SPIRE bands seg-

regates the most massive galaxies. The values of the stellar mass of our PACS-detected LBGs are similar to the stellar masses of LBGs at $z \sim 3$ detected in IRAC 8 μm and MIPS 24 μm (Magdis et al. 2010a).

Differences between PACS-detected and PACS-undetected LBGs. In order to examine the differential properties between PACS-detected and PACS-undetected LBGs, we plot in Fig. 8 the distribution of UV luminosities, UV continuum slope, age, dust attenuation, stellar mass and specific SFR ($sSFR = SFR/M_*$) for the PACS-undetected LBGs with black dashed histograms. It can be seen that, as could be expected from Fig. 3, PACS-undetected LBGs are intrinsically UV-brighter and less attenuated, have lower stellar mass and present bluer UV continuum slopes than their PACS-detected analogues. However, there is no remarkable difference in age or sSFR. The no correlation with age is in agreement with Fig. 3. The median values of the distributions of PACS-undetected LBGs are $\log(L_{UV}/L_{\odot}) = 9.72$, $\beta = -1.55$, Age = 341 Myr, $E_s(B-V) = 0.2$, $\log(M_*/M_{\odot}) = 9.91$ and $\log(sSFR[Gyr^{-1}]) = 0.46$.

3 DUST ATTENUATION

Part of the light emitted by galaxies in the UV is absorbed by dust and re-emitted in turn in the FIR. Therefore, the most accurate way to obtain dust attenuation of galaxies is comparing the total IR and rest-frame UV luminosities. In fact, calibrations between the dust attenuation and the L_{IR}/L_{UV} ratio have been already built. To obtain the dust attenuation of our PACS-detected galaxies, we use the calibration of Buat et al. (2005):

$$A_{FUV} = -0.0333x^3 + 0.3522x^2 + 1.1960x + 0.4967, \quad (2)$$

where A_{FUV} is the dust attenuation in the FUV band and $x = \log(L_{IR}/L_{UV})$. The conversion from A_{FUV} to the dust attenuation in 1200 Å, $A_{1200\,\text{Å}}$, is made by using the Calzetti et al. (2000) reddening law. Fig. 9 shows the dust attenuation of our PACS-detected
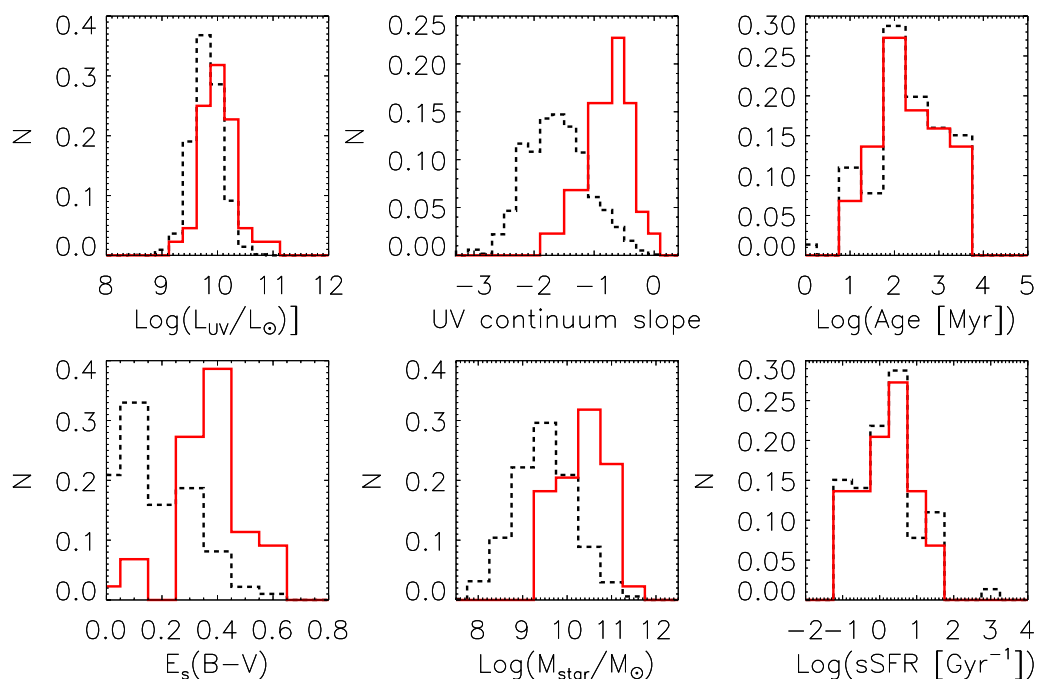

Figure 8. Distribution of the SED-derived rest-frame UV luminosity (upper left), UV continuum slope (upper middle), age (upper right), dust attenuation (bottom left), stellar mass (bottom middle) and sSFR (bottom right) for our PACS-detected LBGs (red histograms) and PACS-undetected LBGs (black dashed histograms). Histograms have been normalized to their area in order to clarify the representations.
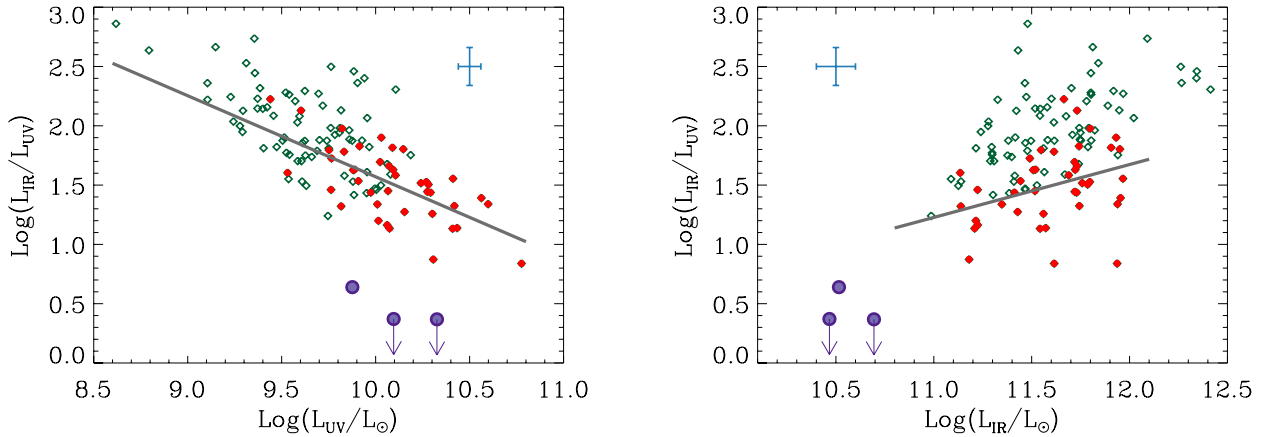
Figure 9. Left: IR/UV ratio (related to dust attenuation through equation 2) as a function of the rest-frame UV luminosity for PACS-detected LBGs (red filled dots) and the general population of UV-selected galaxies (green open diamonds). Right: IR/UV ratio as a function of the total IR luminosity for PACS-detected LBGs (red filled dots) and UV-faint galaxies (green open diamonds). In both panels, the grey solid lines represent a linear fit to the PACS-detected LBGs. PACS-stacked LBGs in the three bins of rest-frame UV luminosity are represented by the filled purple dots. The arrows indicate the two bins of rest-frame UV luminosity where no stacked detections are recovered. The blue error bars indicate the typical uncertainties of the parameters shown in the horizontal and vertical axes.

LBGs (red dots) and UV-faint galaxies (green open triangles) as parametrized by their L_{IR}/L_{UV} ratio (Buat et al. 2005) as a function of their L_{UV} and L_{IR}. PACS-detected LBGs have dust attenuation spanning $2 \lesssim A_{1200\,\text{Å}}[\text{mag}] \lesssim 5$, with a median value of 3.6 mag. In the comparison between LBGs and UV-faint galaxies, Fig. 9 indicates that LBGs tend to be among the less dusty objects in our sample of PACS-detected galaxies. The median value of dust attenuation of our PACS-detected UV-faint galaxies is $A_{1200\,\text{Å}} = 4.3$ mag. The difference in dust attenuation is a consequence of the UV and IR luminosities: LBGs are UV-brighter and have similar IR luminosities than UV-faint galaxies, implying that they are also less dustier according to the Buat et al. (2005) calibration.

There seems to be a tight trend between the dust attenuation and the rest-frame UV luminosity: the dust attenuation decreases when the rest-frame UV luminosity increases (see the left-hand panel of Fig. 9). A similar result was reported by Burgarella et al. (2011) for their SPIRE-detected LBGs and by Buat et al. (2012) at higher redshifts. We have fitted a linear relation to the dust attenuation and rest-frame UV luminosity of PACS-detected LBGs, shown in Fig. 9 with a grey straight line. This relation, although fitted for PACS-detected LBGs only, is also followed by the PACS-detected UV-faint galaxies. This tendency should be understood as valid for the envelope corresponding to highest values of dust attenuation, since we are only considering FIR-detected galaxies and this selection tends to segregate the dustiest galaxies at $z \sim 1$. We also show in the left-hand panel of Fig. 9 the three points corresponding to the stacking of the galaxies in three bins of rest-frame UV luminosities. The stacked points suggest that when introducing FIR-fainter galaxies, the relation between the dust attenuation and the rest-frame UV luminosity has a much higher spread and, therefore, that relation is a direct consequence of the FIR-selection effect.

On the IR side, there also seems to be a trend between the dust attenuation and the total IR luminosity in the sense that more IR-luminous PACS-detected LBGs are dustier (see the right-hand panel of Fig. 9). We have also fitted here a linear relation for the PACS-detected LBGs, shown with the grey straight line. However, in this case PACS-detected UV-faint galaxies do not follow that relation but they tend to be located above it and, therefore, for the same IR luminosity, PACS-detected UV-faint galaxies tend to have higher values of dust attenuation than PACS-detected LBGs. This is again

a direct consequence of the similarity in the IR luminosities and the difference in the rest-frame UV brightness between the two kinds of galaxies. Interestingly, in this case the stacked points associated with the three bins of rest-frame UV luminosity do tend to follow the linear relation fitted for PACS-detected LBGs although with some deviation towards lower values of dust attenuation. This might indicate that when including FIR-fainter galaxies, the correlation between the dust attenuation and the total IR luminosity still holds. We show with a dashed grey straight line a linear fit to the points corresponding to both the PACS-detected LBGs and the PACS-stacked ones.

3.1 Bolometric luminosity and dust attenuation

Fig. 10 shows the bolometric luminosity against dust attenuation for our PACS-detected LBGs and UV-faint galaxies at $z \sim 1$. In order to compare the behaviour of UV-selected galaxies at different redshifts, we also consider a sample of PACS-detected galaxies at $0.2 \lesssim z \lesssim 0.4$. This sample is built by considering that all the galaxies in the COSMOS field which are detected both in GALEX and PACS (100 or 160 µm) and whose photometric redshifts taken from the COSMOS survey (Capak et al. 2007) indicate that they are at $0.2 \lesssim z \lesssim 0.4$. This sample is included in Fig. 10 with small yellow open dots. The dissimilar range of rest-frame UV luminosities between the samples of UV-selected galaxies at different redshifts is due to their selection criteria: at higher redshifts only the brightest galaxies are selected. Therefore, with the aim of comparing samples at different redshifts, their rest-frame UV luminosities must be limited to the same range to avoid any UV selection bias. In our case, the sample at $z \sim 0.3$ contains galaxies with lower rest-frame UV luminosities than the sample at $z \sim 1$. Therefore, we have to limit the sample at $z \sim 0.3$ to the same rest-frame UV luminosity range as the galaxies at $z \sim 1$. It can be seen in Fig. 6 that the number of PACS-detected UV-selected galaxies at $z \sim 1$ significantly drops for $\log(L_{UV}/L_\odot) \lesssim 9.4$. Thus, we only take into consideration in this analysis those galaxies both at $z \sim 1$ and $z \sim 0.3$ whose rest-frame UV luminosities are above that value. The zone in Fig. 10 which satisfies that condition is shaded in grey.

Focusing first on the galaxies at $z \sim 1$, Fig. 10 indicates that there might be a relation between the bolometric luminosity and the
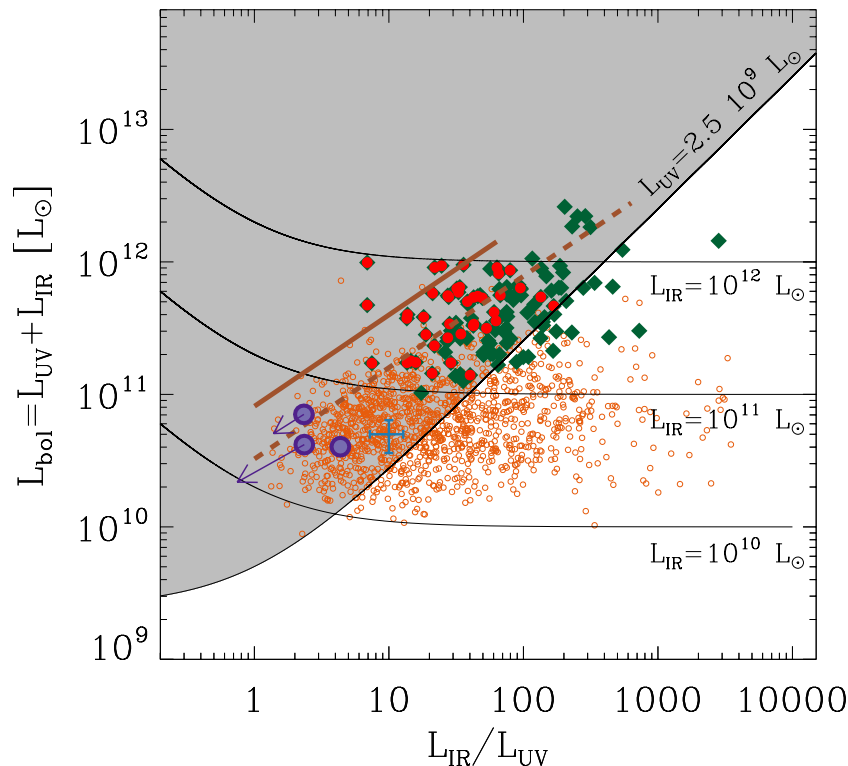
Figure 10. Bolometric luminosity as a function of the dust attenuation parametrized by the IR/UV ratio. PACS-detected LBGs and the general population of UV-selected galaxies are represented by red dots and green diamonds, respectively. A sample of UV-selected galaxies at $z \sim 0.3$ with UV and PACS measurements is also represented by yellow open dots. The black curves indicate different constant values of the rest-frame UV and total IR luminosities. The value chosen for the rest-frame UV luminosity is $\log(L_{UV}/L_\odot) = 9.2$, which is the minimum typical value for our PACS-detected galaxies at $z \sim 1$ (see the text for more details). The grey shaded zone represents the location of the galaxies with rest-frame UV luminosity above that threshold. The values chosen for the total IR luminosity are those differentiating the three main kinds of FIR-selected galaxies: normal SF galaxies, LIRGs and ULIRGs: $L_{IR} = 10^{10}$, 10^{11} and $10^{12} L_\odot$, respectively. We also include in the plot the bolometric luminosities and IR/UV ratios associated with the stacked points in the three bins of rest-frame UV luminosity with purple filled dots. The arrows indicate upper limits for the two ranges where no stacked detections are recovered. The solid brown line denotes the Reddy et al. (2010) relation between the bolometric luminosity and the dust attenuation for galaxies at $z \sim 2$. The dashed brown line is plotted to guide the eye about the relation between the bolometric luminosity and the dust attenuation for our PACS-detected galaxies. It has the same slope as the relation of Reddy et al. (2010) but the zero-point is 2.5 times lower. The blue error bars indicate the typical uncertainties of the parameters shown in the horizontal and vertical axes.

dust attenuation for galaxies with $\log(L_{UV}/L_\odot) \geq 9.4$ in the sense that higher values of dust attenuation correspond to higher values of the bolometric luminosity. However, the scatter is significant, about 0.45 dex. Such a correlation between those variables has also been reported in other works at similar (Buat et al. 2009) and higher redshifts (Reddy et al. 2010). At $z \sim 2.0$, Reddy et al. (2010) found a strong relation between L_{bol} and dust attenuation with a scatter of 0.23 dex about a linear fit, which is very similar to the trend found in Reddy et al. (2006). This relation is plotted in Fig. 10 with a continuous brown line. It should be pointed out that in the derivation of such a relation, they included both MIPS-detected and MIPS-undetected galaxies and, given that they work with galaxies at $z \sim 2$, their UV luminosities tend to be higher than those for our PACS-detected galaxies and therefore their galaxies are bolometrically more luminous than ours. Despite these differences, our points tend to follow a linear relation with a similar slope than that found in Reddy et al. (2010) but with a lower zero-point due to the difference in the rest-frame UV luminosity between the two samples. Only the least dusty and most bolometrically luminous PACS-detected LBGs at $z \sim 1$ are in agreement with the Reddy et al. (2010) relation. We plot in Fig. 10 with a brown dashed line a linear relation with the same slope as that in Reddy et al. (2010) but with the bolometric luminosities divided by a factor of 2.5. It can be

seen that this relation is well followed by the PACS-detected LBGs and also by the stacked LBGs in PACS 160 μm associated with the three ranges of the rest-frame UV luminosity. Furthermore, the PACS-detected galaxies at $z \sim 0.3$ with $\log(L_{UV}/L_\odot) \geq 9.4$ tend to follow the same relation as our LBGs at $z \sim 1$, filling in the $L_{bol}-L_{IR}/L_{UV}$ diagram the gap between our PACS-detected and PACS-stacked LBGs.

Considering the whole sample of UV- and FIR-detected galaxies at $z \sim 0.3$ regardless of the rest-frame UV luminosities, it can be seen that there is a large spread in the relation between the bolometric luminosity and the dust attenuation of these galaxies. That spread prevents us from formulating any relation between the bolometric luminosity and the dust attenuation. In the analysis at $z \sim 1$, we cut the rest-frame UV luminosity of the galaxies to $\log(L_{UV}/L_\odot) \geq 9.4$ and obtain that, with that limitation, there is a relation between L_{bol} and L_{IR}/L_{UV} although with the same scatter. The large scatter at $z \sim 0.3$ makes us speculate that the relation found at $z \sim 1$ is only a consequence of the cut in the rest-frame UV luminosity and also in the total IR luminosity (a consequence of the PACS limiting fluxes in the COSMOS field). If we could go deeper in the rest-frame UV and IR luminosity functions, both at $z \sim 1$ and at higher redshifts, the relation between the bolometric luminosity and the dust attenuation would not be so clear.

3.2 Dust attenuation and UV continuum slope

Part of the light emitted by galaxies in the UV is absorbed by dust. This absorption takes place in a wavelength-dependent way: bluer wavelengths are more attenuated than redder ones. This selective attenuation implies a change in the UV continuum slope with dust attenuation: for a given age, SFH, metallicity, and when the dust attenuation increases, bluer zones of the UV continuum are more attenuated than redder zones, producing an increase of the UV continuum slope, β, from negative to less negative or even positive values. Furthermore, as has been commented before, the absorbed light by dust in the UV is in turn re-emitted in the FIR, and the ratio between the total IR and rest-frame UV luminosities is the best tracer of dust attenuation. Therefore, the UV continuum slope and dust attenuation could be correlated: higher (redder) values of the UV continuum slope could be due to higher values of dust attenuation. However, it should also be considered that the relation between the UV continuum and dust attenuation could be partially hidden by the presence of evolved stellar populations, which also tend to redden the UV continuum of galaxies.

The UV continuum slope is a quantity relatively easy to determine since it only requires a good sampling of the rest-frame UV continuum, which is usually achieved for galaxies in a wide range of redshifts (Bouwens et al. 2006, 2009, 2012; Hathi, Malhotra & Rhoads 2008; Wilkins et al. 2011; Finkelstein et al. 2012; Hathi et al. 2013). However, the accurate measurement of dust attenuation, mostly at high redshift, is very challenging since it requires information of the dust emission in the FIR. In the local, low- and intermediate-redshift universe, a relatively high percentage of galaxies exhibit observed FIR fluxes high enough to be detected with current instrumentation. However, in the high-redshift universe, a very low percentage of galaxies are individually detected in the FIR and, therefore, the accurate determination of dust attenuation is only possible for some of the IR-brightest sources. This is one of the main reasons why many authors try to recover the dust attenuation from the values of the UV continuum slope by using some relations between the UV slope and dust attenuation, the so-called IRX–β relations (see for example Meurer, Heckman & Calzetti 1999; Boissier et al. 2007; Boquien et al. 2009, 2012; Murphy et al. 2011; Overzier et al. 2011; Buat et al. 2012; Wilkins et al. 2012; Heinis et al. 2013).[1] The IRX–β relations that are found in the literature have been defined for a specific kind of galaxies at specific redshifts. This is the case, for example, of local SB (Meurer et al. 1999, hereafter M99) or local SF galaxies (Boissier et al. 2007, hereafter B07).

However, the IRX–β relation has been proven not to be tight for any kind of galaxies. Goldader et al. (2002) obtained that the SB relation does not reproduce the observed IRX–β relation for local LIRGs and ULIRGs. These galaxies tend to be located above the SB curve: for a given UV continuum slope, local LIRGs and ULIRGs tend to have higher dust attenuation than that predicted by the SB relation (Buat et al. 2005; Takeuchi et al. 2010). For FIR-bright galaxies at $z \sim 0.3$, there is no clear IRX–β relation either, since they are located over a wide region of the IRX–β diagram (Buat et al. 2010; Oteo et al. 2012b). Nordon et al. (2013) find that main-sequence (MS) galaxies form a tight sequence in the IRX–β diagram, which has a flatter slope than the commonly used relation and favours an Small Magellanic Cloud-like UV extinction curve. Furthermore, they also find that the location of galaxies in

the IRX–β diagram correlates with their location in the SFR–M_* diagram. Additionally, Reddy et al. (2012) suggest that the location of galaxies in the IRX–β diagram depends upon age; younger galaxies follow a relation that is stepper than the M99 and Calzetti et al. (2000) ones.

In this section, by analysing the location of our PACS-detected galaxies at $z \sim 1$ in an IRX–β diagram (see Fig. 11), we examine whether they follow a relation between the dust attenuation and β and, therefore, whether it is possible to recover their dust attenuation from their UV continuum slope in an accurate way. In Fig. 11, our PACS-detected LBGs are represented with red dots and our PACS-detected UV-faint galaxies with green open triangles. The curves of M99 and B07 for local SB and SF galaxies, respectively, are also shown. We also represent the correction of Takeuchi et al. (2012, hereafter T12) to the M99 law that takes into consideration the small aperture of *IUE* that may have missed about half of the light (see also Overzier et al. 2011). It can be seen that our PACS-detected LBGs are mostly distributed around the M99 relation and within the zone defined by the uncertainties in the IRX ratio of the M99 relation (orange shaded zone). This also applies for our PACS-detected UV-faint galaxies. The location of our PACS-detected galaxies is also compatible with the Buat et al. (2012) relation for PACS-detected UV-selected galaxies at $0.95 < z < 2.2$. Heinis et al. (2013) obtain an IRX–β relation for galaxies at $z \sim 1.5$ that, for a given UV continuum slope, gives lower values of the dust attenuation than those of our PACS-detected LBGs. This is likely due to the higher redshifts of their sources and mainly to the stacking analysis employed in that work that allows the authors to recover less dusty galaxies.

In Fig. 11, we also include the points associated with the stacked PACS 160 μm fluxes for our LBGs in the six bins of rest-frame UV luminosities, stellar mass and age. The UV continuum slope in each bin is the median value of the galaxies included in each one. As expected from Figs 3 and 8, the PACS-stacked LBGs (which are PACS-undetected) are bluer than the PACS-detected LBGs and, therefore, are located in a different zone of the IRX–β diagram. In the two cases where a stacked detection is recovered, we obtain that the point follows the M99 relation, although the upper values in the cases where a stacked detection is not recovered indicate that the actual dust attenuation is lower than that predicted by the M99 law, favouring the T12 relation. In the zone where the stacked points are located, the M99, B07 and T12 curves are very close to each other. Actually, the B07 law is contained within the uncertainty region associated with the M99 relation. Therefore, any of the laws might be used to recover the dust attenuation of those galaxies from their UV continuum slope.

For a given value of the UV continuum slope, PACS-detected LBGs tend to have slightly lower values of dust attenuation than PACS-detected UV-faint galaxies. This is a direct consequence of the different selection criterion since LBGs are among the most UV-luminous galaxies and, therefore, have lower values of the IRX ratio. Furthermore, it can be seen in Fig. 11 that PACS-detected LBGs tend to be located in a zone of the IRX–β diagram corresponding to bluer values of the UV continuum slope than PACS-detected UV-faint galaxies. In this way, we obtain that UV-brighter PACS-detected galaxies have bluer UV continuum slopes. At higher redshifts, Finkelstein et al. (2012) do not find a significant correlation ($\lesssim 2\sigma$) between both parameters within $z \sim 4$–7. Dunlop et al. (2012) do not find a significant trend between the UV continuum slope and the rest-frame UV luminosity within $z = 5$–7. However, Bouwens et al. (2012) report the existence of a well-defined rest-frame UV colour–magnitude relation that becomes systematically bluer when the UV luminosity decreases. Bouwens et al. (2009)

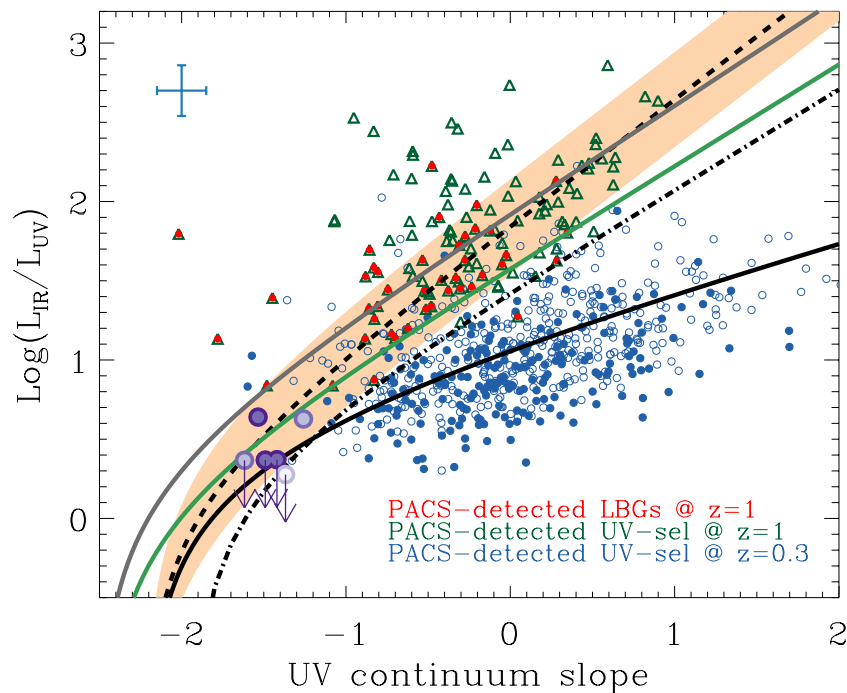
[1] IRX refers to $\log(L_{IR}/L_{UV})$.

Figure 11. Dust attenuation parametrized by the IR/UV ratio (IRX) as a function of the UV continuum slope for our PACS-detected LBGs and UV-selected galaxies, represented by red filled dots and green open triangles, respectively. For comparison, we also represent a sample of UV-selected PACS-detected galaxies at $z \sim 0.3$ with blue filled dots for galaxies with $\log(L_{UV}/L_{\odot}) \geq 9.8$ and with blue open dots for galaxies with $\log(L_{UV}/L_{\odot}) < 9.8$. The dashed curve represents the M99 law for local SB, the dashed dotted curve shows the correction of Takeuchi et al. (2012) to the M99 law and the continuous line denotes the curve of B07 for normal local SF galaxies. The shaded region represents the dispersion of IRX around the M99 law. The IRX–β relations of Buat et al. (2012) and Heinis et al. (2013) are overplotted with grey and green solid curves, respectively. We also plot with purple filled dots the points corresponding to the staked PACS 160 μm fluxes for the six bins considered in the stacking procedure (see the text for more details). The arrows indicate upper limits for the bins where no stacked detections are recovered. The blue error bars indicate the typical uncertainties (taken from Oteo et al. 2013a) of the parameters shown in the horizontal and vertical axes.

obtain a similar behaviour within $z = 2.5$–4. Castellano et al. (2012) report that brighter LBGs at $z \sim 4$ are only slightly redder than fainter ones. Therefore, there seems to be some discrepancy in the results. What we have obtained for our PACS-detected LBGs and UV-faint galaxies does not apply to the whole population of SF galaxies at $z \sim 1$ since we have only considered the FIR-brightest galaxies. We further analyse the situation in Fig. 12 including the PACS-undetected LBGs as well. As expected from Fig. 8, for each value of the rest-frame UV luminosity, PACS selects the reddest galaxies in the UV continuum. Furthermore, it can be seen that the trends found for PACS-detected and PACS-undetected galaxies are completely different as a consequence of their different FIR nature. Whereas for PACS-detected galaxies there is a clear reddening at lower luminosities, the median values of the UV continuum slope associated with the PACS-undetected galaxies seem to become bluer with decreasing luminosity. However, it should be remarked that the width of the distributions of the UV continuum slope for each bin of luminosity is high and, therefore, no correlation can be significantly constrained. Finally, it is also interesting to point out that the values of the UV continuum slope of our LBGs and UV-faint galaxies (both PACS-detected and PACS-undetected) are higher than those obtained in Finkelstein et al. (2012) and Bouwens et al. (2009, 2012), indicating an evolution of the UV continuum slope from $z \sim 7$ down to $z \sim 1$ (see also Oteo et al. 2013a).

Location of galaxies in the IRX–β diagram as a function of redshift. We compare now the location in the IRX–β diagram of UV-selected PACS-detected galaxies as a function of redshift, focusing on our PACS-detected galaxies at $z \sim 1$ and $z \sim 0.3$. We use here the same sample of UV-selected galaxies at $z \sim 0.3$ as in Section 3.1. Note that this sample is limited to the same rest-frame UV luminosity as the UV-selected galaxies at $z \sim 1$ and, therefore, there is no bias in their UV selection. However, there is a bias in the IR selection since at $z \sim 0.3$ we can detect less IR luminous sources and this may have an effect on their dust properties. There is an additional difference between the two samples, which is the calculation of the UV continuum slope. As indicated in Oteo et al. (2013a), the UV continuum slope for the galaxies in our sample of UV-selected galaxies at $z \sim 1$ is obtained by fitting a power law to the templates which fit the *GALEX*+ALHAMBRA photometry of each galaxy best. For the galaxies at $z \sim 0.3$, we do not have such a high-quality photometric coverage of the UV continuum and, as a consequence, their UV continuum slope is obtained from their photometry in the FUV and NUV bands as in Kong et al. (2004), Buat et al. (2010) or Oteo et al. (2012b), for example. Fig. 10 indicates that galaxies at $z \sim 0.3$ are located mostly around the SF relation. This represents a difference between $z \sim 1$ and $z \sim 0.3$ and implies that for a given value of the UV continuum slope, the dustiest galaxies at $z \sim 0.3$ are less attenuated than the dustiest UV-selected galaxies at $z \sim 1$. This tendency seems to continue to higher redshifts. According to Oteo et al. (2013b), PACS-detected LBGs at $z \sim 3$ are more attenuated than PACS-detected LBGs at $z \sim 1$ for a given UV continuum slope. This higher dust attenuation for galaxies at higher redshifts might be due to an evolution of the IR luminosity of LBGs with redshift, at least in the IR-bright envelope. The dust attenuation recovered from the stacking analysis for the PACS-undetected LBGs at $z \sim 1$ is as low as the values found for galaxies at $z \sim 0.3$. However, they tend
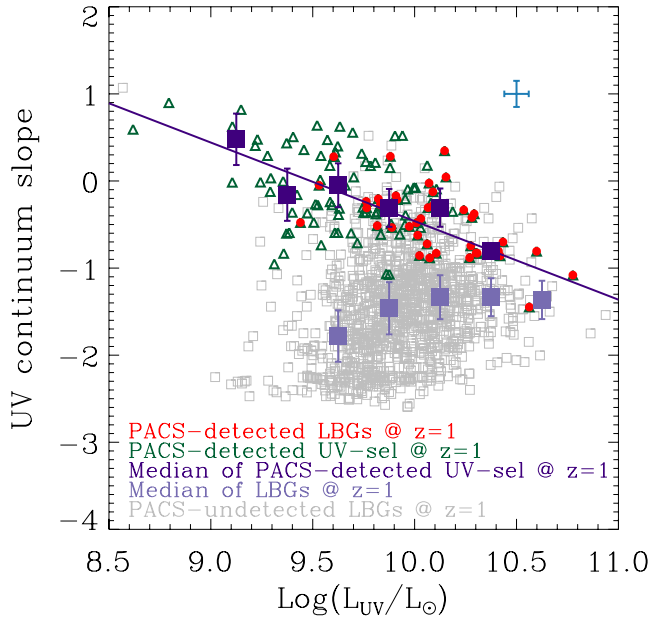
Figure 12. Relation between the UV continuum slope and the rest-frame UV luminosity of our PACS-detected LBGs (red dots) and PACS-detected UV-faint galaxies (green open triangles). The filled dark purple squares represent the median value of the UV continuum slope of the PACS-detected galaxies in different bins of rest-frame UV luminosity, the error bars being the width of the distributions. The solid dark purple line shows a linear fit to the dark purple filled squares. For comparison, we also represent the PACS-undetected LBGs at $z \sim 1$ with grey open squares. The filled light purple squares represent the median value of the UV continuum slope of PACS-undetected galaxies in different bins of rest-frame UV luminosity, the error bars being the width of the distributions. The blue error bars indicate the typical uncertainties of the parameters shown in the horizontal and vertical axes.

to be located in a zone of IRX–β diagram associated with much bluer values of the UV continuum slope. This might indicate that, for the same dust attenuation, galaxies at higher redshifts tend to have bluer values of the UV continuum slope than galaxies at lower redshifts.

Combining all previous results, it turns out that the location of UV-selected galaxies in the IRX–β depends upon the rest-frame UV luminosity, total IR luminosity and redshift. Therefore, in general, dust attenuation for UV-selected galaxies at $z \sim 1$ cannot be recovered from the UV continuum slope with a single dust attenuation law. It should be noted that this result only applies for FIR-detected galaxies. For those FIR undetected, we can only give an approximation to their location in the IRX–β diagram throughout the stacking analysis and, therefore, the application of a single relation between the UV continuum slope and the dust attenuation is even riskier.

4 STAR FORMATION RATE

There are some estimators of the SFR in galaxies, such as Hα emission, UV emission, IR emission or radio continuum. May be, the best determination of the total SFR in galaxies can be obtained by combining UV and FIR emissions, since they represent the measured UV light and the emission in the FIR of the light which is absorbed in the UV by dust, respectively. In this way, the total SFR, SFR_{total}, can be obtained by summing the star formation associated with the rest-frame UV light uncorrected by dust absorption,
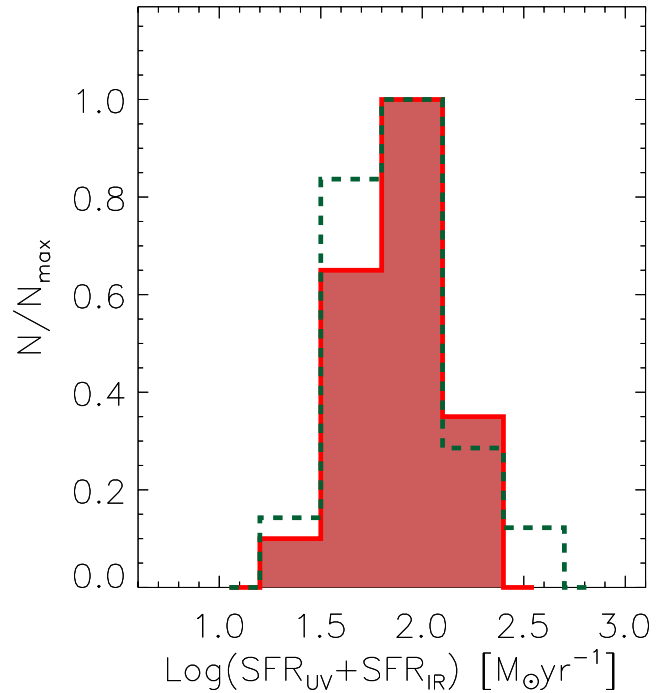
Figure 13. Distribution of the total SFR as derived from the combination of UV and IR emissions for the galaxies studied in this work. PACS-detected LBGs and UV-selected galaxies are represented by red shaded and dashed green histograms. Histograms have been normalized to clarify the representation.

$SFR_{UV, uncorrected}$, and the star formation associated with the emitted IR light, SFR_{IR}. Each one can be obtained independently from the rest-frame UV and total IR luminosities by applying the Kennicutt (1998) calibrations:

$$SFR_{UV,uncorrected}[M_\odot\,yr^{-1}] = 1.4 \times 10^{-28} L_{1500} \qquad (3)$$

$$SFR_{IR}[M_\odot\,yr^{-1}] = 4.5 \times 10^{-44} L_{IR}, \qquad (4)$$

where the IR luminosity is defined in the same way as in Section 2.1 and L_{1500} is defined in an L_ν way. The total SFR can be obtained from

$$SFR_{total} = SFR_{UV,uncorrected} + SFR_{IR}. \qquad (5)$$

Fig. 13 represents the distribution of the total SFR for our sample of PACS-detected galaxies. The median values for our PACS-detected LBGs and UV-faint galaxies are 91 ± 22 and 73 ± 39 $M_\odot\,yr^{-1}$, respectively. The uncertainties correspond to the standard deviation of the distributions, as a measure of their width. Therefore, PACS-detected LBGs have higher values of the total SFR than UV-faint galaxies.

4.1 Dust-correction factors at $z \sim 1$

In the upper panel of Fig. 14, we represent the SED-derived dust-corrected total SFR against the total SFR obtained from the combination of UV and IR measurements (equation 5) for our PACS-detected LBGs (red dots) and UV-selected galaxies (green triangles). We define the SED-derived total SFR as the one obtained by multiplying the rest-frame dust-uncorrected $SFR_{UV,uncorrected}$ by the factor $10^{0.4A_{1500}}$, where A_{1500} is the dust attenuation in 1500 Å calculated from the SED-derived $E_s(B-V)$ assuming the Calzetti
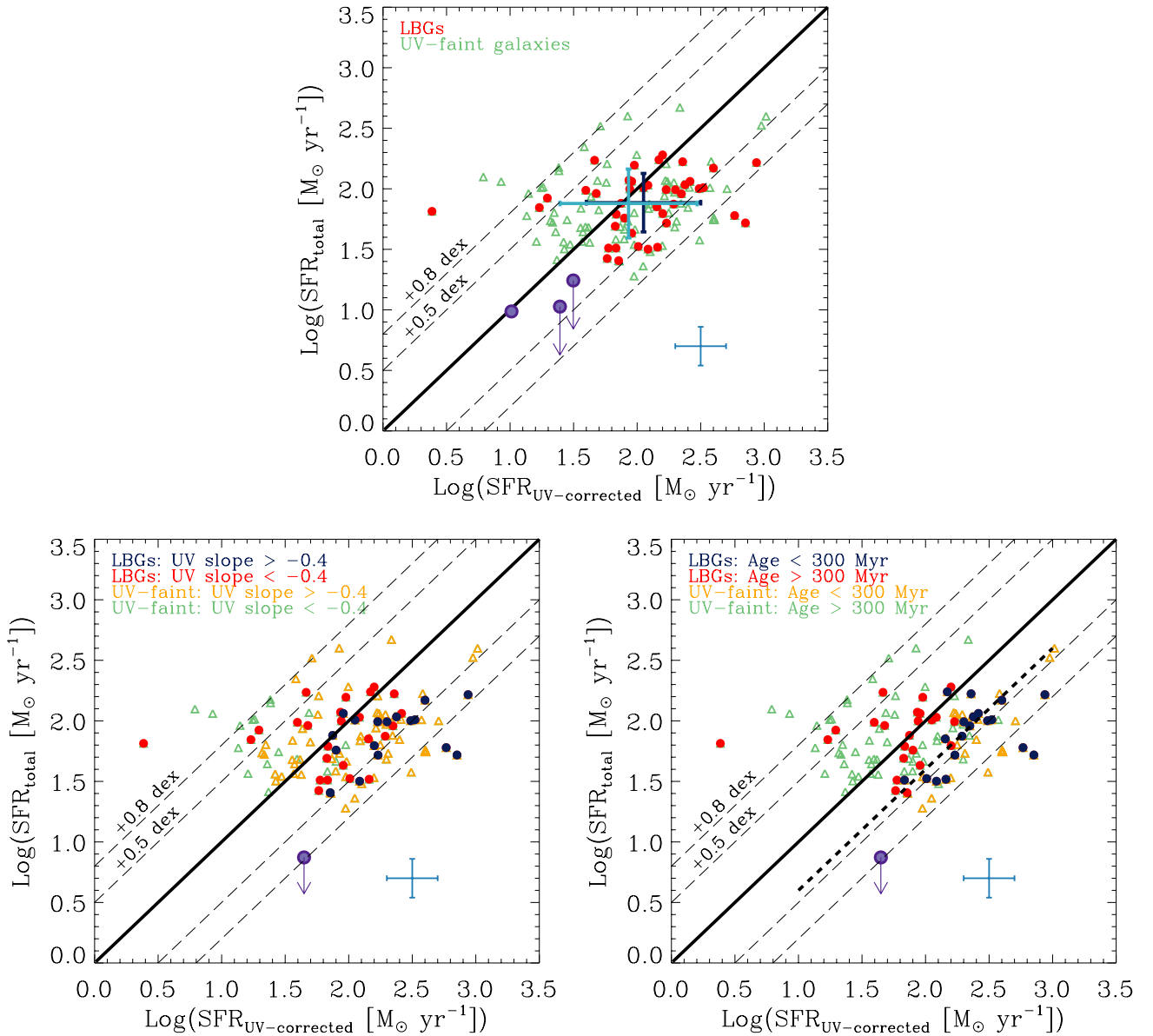
Figure 14. Top: total SFR derived from the combination of UV and FIR measurements against the total SFR derived by correcting the rest-frame UV luminosity with the SED-derived $E_s(B − V)$ value obtained from SED fitting with BC03 templates associated with a constant SFR and constant sub-solar metallicity $Z = 0.4\,Z_{\odot}$. PACS-detected LBGs and UV-selected galaxies are represented by red filled dots and green open triangles, respectively. The solid line shows the one-to-one relation. The median loci in the diagram of the PACS-detected LBGs and UV-selected galaxies are represented by the dark blue and light blue bars, respectively. The bars cross in the average value of each parameter for each kind of galaxy and the length of the bars is the standard deviation of the distribution of values. We denote with purple filled dots the point corresponding to the stacking in the three bins of rest-frame UV luminosity. The arrows indicate upper limits for the two ranges where no stacked detections are recovered. The blue error bars indicate the typical uncertainties (taken from Oteo et al. 2013a) of the parameters shown in the horizontal and vertical axes. Bottom left: the same as in the top panel but different points corresponding to LBGs and UV-faint galaxies with different values of the UV continuum slope, as indicated. The red and blue filled dots represent PACS-detected LBGs, while the green and orange open triangles represent the general population of UV-selected galaxies. Bottom right: the same as bottom left but different values of age, as indicated. The dashed straight line indicates a deviation of $−0.6$ dex with respect to the one-to-one relation (solid line) and it is represented to guide the eye about the overestimation of the SED-derived total SFR for young galaxies. We plot in the bottom-right and left-hand panels the upper value corresponding to the stacked PACS 160 μm flux of the galaxies younger than 100 Myr with a purple filled dot.

et al. (2000) law. We also represent the median loci of each kind of galaxy in the diagram. It can be seen that, although in average the SED-derived dust attenuation reproduces the UV+IR-derived total SFR with some underestimation, the dispersion around the one-to-one relation is relatively high. We also include in that panel the points associated with the stacking analysis in the three bins of rest-frame UV luminosity. It can be seen that there is good agree-

ment between the SED-derived and UV+IR-derived total SFRs, although the PACS-stacked points associated with the highest values of the rest-frame UV luminosity are more deviated from the one-to-one relation, suggesting again that the SED-derived $E_s(B − V)$ gives overestimated results of the total SFR for UV-bright galaxies. This is opposite to what is found at $z \sim 3$, where the SED-derived $E_s(B − V)$ underestimates the total SFR for most PACS-detected
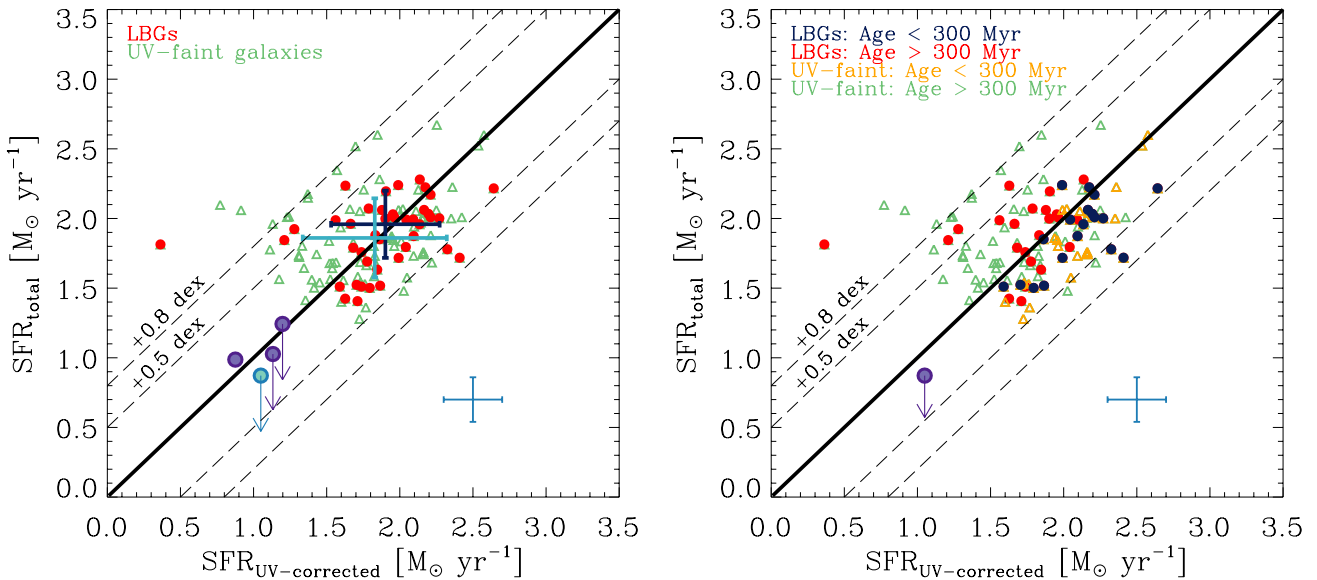
Figure 15. Left: total SFR derived from the combination of UV and IR measurements against the total SFR obtained by correcting the rest-frame UV luminosity with the UV continuum slope and applying M99 relation. PACS-detected LBGs and UV-selected galaxies are represented with red filled dots and green open triangles, respectively. The median loci in the diagram of the PACS-detected LBGs and UV-selected galaxies are represented by the dark blue and light blue bars, respectively. The bars cross in the median value of each parameter for each kind of galaxy and the length of the bars is the standard deviation of the distribution of values. The solid line shows the one-to-one relation. PACS-stacked LBGs in the bins of rest-frame UV luminosity are represented as filled purple dots and the PACS-stacked LBGs in the age bin are indicated with a filled blue dot. The arrows indicate upper values where no stacked detection is found. The blue error bars indicate the typical uncertainties (taken from Oteo et al. 2013a) of the parameters shown in the horizontal and vertical axes. Right: the same as in the left-hand panel but considering different IRX relations: M99 in green, Overzier et al. (2011) in orange and T12 in purple. In this plot, and with the aim of clarifying the results, LBGs and UV-faint galaxies are considered as a whole population.

LBGs. It should be remarked that the fact that the uncertainties in the SED-derived and UV+IR-derived total SFR are very similar does not mean, a priori, that the SED-derived is as good an estimator of the total SFR as the UV+IR-derived. The uncertainties in the SED-derived total SFR only reflect the uncertainties in the SED-derived dust attenuation and rest-frame UV luminosity but do not reflect the capacity of the SED-fitting procedure to reproduce the FIR emission of the galaxies. There are some physical reasons from that we expect that the UV+IR-derived total SFR is a good estimator of the real total SFR of a galaxy, but there is no physical reason to expect that it is possible to recover the total SFR for any kind of galaxy. This is only an expectation from the SED-fitting procedure employed, but it is something that needs to be checked.

In the lower panels of Fig. 14 we further analyse the relation between SED-derived and UV+IR-derived total SFRs by dividing the sample of PACS-detected galaxies as a function of the UV continuum slope and the SED-derived age of the galaxies. It can be seen that the PACS-detected LBGs and UV-faint galaxies which are further the one-to-one relation are those with younger stellar populations. The stacked point corresponding to the galaxies with age younger than 100 Myr is also in agreement with the previous tendency. However, we do not find a significant correlation with the UV continuum slope. It should be noted that the tendency with age can be a consequence of the degeneracy between the dust attenuation and the stellar age in the SED-fitting procedures. The reddening of the SED of a galaxy can be caused either by the presence of an old stellar population or by the presence of high values of dust attenuation. A galaxy with a red SED can be young and dusty but also old and less dusty. In this way, the overestimation of the total SFR for young galaxies, produced by high values of the dust attenuation, can be due to the fact that the SED fitting cannot distinguish between old and young and dust-free and old galaxies.

In the left-hand panel of Fig. 15, we represent the SED-derived dust-corrected total SFR obtained from the dust attenuation derived from the values of the UV continuum slope of each galaxy by employing the M99 law. The accuracy of this method is directly related to the location of our PACS-detected galaxies in the IRX–β diagram. When dust-correcting with this method, the SED-derived dust-corrected total SFR of PACS-detected LBGs and UV-selected galaxies is in very good agreement with the one derived from IR and UV measurements. The points associated with the PACS-stacked galaxies in the three bins of rest-frame UV luminosities are also very near to the one-to-one relation. Comparing the median loci of our PACS-detected galaxies in Figs 14 and 15, it can be seen that the dust attenuation derived from the UV continuum slope and the M99 relation gives much better estimations of the total SFR than that derived with the SED-derived $E_s(B - V)$. As will be explained in Section 8, this differential behaviour is also found when obtaining the total SFR with radio-VLA data instead of FIR ones. The right-hand panel of Fig. 15 shows evidence that the dust-correction factors obtained with the M99 law are also age dependent. Younger galaxies than 300 Myr tend to be located below the one-to-one relation, whereas older galaxies tend to be located above. This might be due to a correlation between age and the location of galaxies in the IRX–β diagram (see also Reddy et al. 2010, 2012).

We compare in Fig. 16 the dust-correction factors obtained after the application of the M99 and the new relations of T12 and Overzier et al. (2011, hereafter O11) for our PACS-detected galaxies. For clarity reasons, we consider in this plot our PACS-detected LBGs and UV-faint galaxies as a whole population of PACS-detected and UV-selected galaxies at $z \sim 1$. It can be seen that the IRX–β relation that represents the best our PACS-detected galaxies is the M99 one. This is a direct consequence of the location of our galaxies in the IRX–β diagram. However, our PACS-detected galaxies represent a
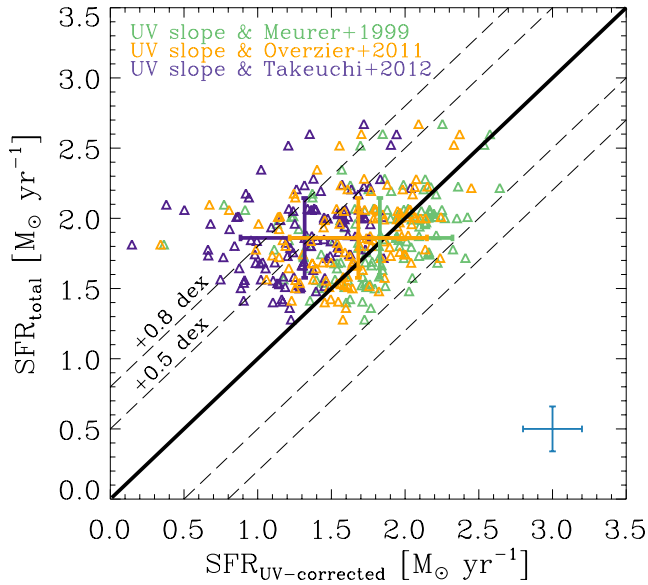
Figure 16. Relation between the UV+IR-derived total SFR and the dust-corrected total SFR by using the UV continuum slope and the application of three different IRX–β relations: the green triangles correspond to the M99 law, the orange triangles to the O11 law and the purple triangles to the T12 law. The median loci of the galaxies in the diagram for each of the three laws are represented with bars of the same colour. The bars cross in the median value of the parameters presented in the x- and y-axes and the length of the bars is the standard deviation of the distribution of values. The solid line shows the one-to-one relation and the dashed lines represent deviations of ± 0.5 and ± 0.8 dex with respect to the one-to-one relation. The blue bars represent the typical uncertainties in the derivation of the total SFR with each of the two methods.

low percentage of the whole population of SF galaxies at $z \sim 1$. Additionally, for each UV slope, PACS only detects the dustiest galaxies. Therefore, an IRX–β relation that gives lower values of the dust attenuation for each UV continuum slope (such as the O11 and T12 ones) might be more appropriate to recover the dust attenuation of SF galaxies at $z \sim 1$ from their UV continuum slope.

5 SFR VERSUS STELLAR MASS DIAGRAM

In Oteo et al. (2013a), we study the location of the whole sample of *GALEX*-selected LBGs in an SFR versus stellar mass diagram (Daddi et al. 2007; Elbaz et al. 2007; Noeske et al. 2007; Salim et al. 2007; Pannella et al. 2009; González et al. 2010; Rodighiero et al. 2010; Elbaz et al. 2011; Karim et al. 2011; Salmi et al. 2012; Sawicki 2012). It was found that, according to the definition of Elbaz et al. (2011) of the MS of galaxies at $z \sim 1$, most *GALEX*-selected LBGs are located in the SB region, giving clues to their SF activity. Additionally, it was found that more massive galaxies have higher total SFR and lower sSFR. In that case, we used SED-derived values of the dust-corrected total SFR, but not those derived from direct IR measurements. Now, we go back to the analysis of the location of our UV-selected galaxies at $z \sim 1$ in the SFR–mass diagram but focusing on the PACS-detected ones and, thus, utilizing the values of the total SFR derived from the combination of UV and IR measurements (equation 5).

The left-hand panel of Fig. 17 represents the SFR−M_* for our PACS-detected LBGs and UV-faint galaxies. The SFRs which appear in the vertical axis of the plot are the total SFRs determined with the combination of UV and IR data (equation 5) and the stellar masses are those obtained by fitting the *GALEX*+ALHAMBRA photometry with BC03 templates built by assuming a constant SFR

Figure 17. Left: location of our PACS-detected galaxies in an SFR–mass diagram. PACS-detected LBGs and UV-selected galaxies are represented with red filled dots and green open diamonds, respectively. The solid black line shows the MS of SF galaxies at $z \sim 1$ taken from Elbaz et al. (2011) and the dashed curve is for twice the values of that MS. The solid grey line shows the MS at $z \sim 1$ of Elbaz et al. (2007). The values of the dust-corrected total SFR adopted are those obtained from the UV continuum slope and the application of the M99 relation (see Section 4.1). The blue error bars indicate the typical uncertainties (taken from Oteo et al. 2013a) of the parameters shown in the horizontal and vertical axes. Right: specific star formation rate, sSFR = SFR/M_* as a function of the stellar mass for our PACS-detected LBGs (red filled dots) and UV-selected galaxies (green open diamonds). The purple filled dots represent the results of the stacking in PACS 160 μm in two bins of stellar mass. The arrow represents the upper limit of the total IR luminosity in the bin associated with the lowest stellar masses, where no stacked PACS 160 μm detection is found. In both panels, for comparison, we also show the location in the SFR–mass and sSFR–mass diagrams of the PACS-undetected LBGs at $z \sim 1$ (grey open squares). The blue error bars indicate the typical uncertainties (taken from Oteo et al. 2013a) of the parameters shown in the horizontal and vertical axes.

(Oteo et al. 2013a). Along with the data points, the SFR–mass relation for the MS of galaxies at $z \sim 1$ (Elbaz et al. 2011) is also represented. Elbaz et al. (2011) assume for their definition of MS a slope of the SFR–mass relation equal to 1 and, therefore, that the sSFR is mass independent at a fixed redshift. First, it can be seen that most PACS-detected galaxies at $z \sim 1$ are over the 'MS' of galaxies at their redshift and, therefore, they are normal SF galaxies. Only the most massive galaxies are below the MS and the less massive are in the SB region. There is no significant relation between SFR_{total} and stellar mass. In Oteo et al. (2013a), we reported that galaxies with higher masses tend to have higher SFRs. The reason why we do not see such a relation here is that in the present work we only analyse PACS-detected galaxies and, therefore a subsample of IR-bright, dusty and massive galaxies of the whole sample analysed in Oteo et al. (2013a). The range of IR luminosities of our galaxies does not allow us to constrain a general relation between SFR_{total} and stellar mass. However, we do see that despite having a narrow range of values of SFR_{total}, there is a large dispersion in the stellar mass values. This result is consistent with that found in Giovannoli et al. (2011) for their MIPS 24 μm selected LIRGs at ~1. They also found that galaxies with stellar populations younger than 300 Myr exhibit a larger dispersion in the stellar mass than galaxies whose SFR is constant over a longer period.

With the aim of gaining insights about the location of IR-faint galaxies in the $SFR - M_*$ diagram, we also plot the two points associated with the stacking results of the galaxies located in the two bins of stellar mass defined in Section 2.2. It can be seen that the stacked point corresponding to the LBGs in the range of the highest stellar masses is right over the MS of galaxies. The upper limit of the total SFR for PACS-stacked LBGs in the range of the lowest values of stellar mass indicates that most of these galaxies might also be located over the MS. This indicates that most *GALEX*-selected LBGs, regardless of their detection in the FIR, tend to be located over the MS of galaxies at their redshift.

We find (see the right-hand panel of Fig. 17) a trend between the sSFR and the stellar mass, which is similar to that found in Oteo et al. (2013a) with UV, optical and near-IR data and in some other works at different redshifts (Feulner et al. 2005a,b; Erb et al. 2006; Damen et al. 2009; Dunne et al. 2009; Rodighiero et al. 2010): galaxies with higher stellar masses tend to have lower sSFRs. This relation is characterized by its slope. In Oteo et al. (2013a), by fitting a linear relation of the form $\log(sSFR[Gyr^{-1}]) = a + b \times \log(M_*[M_\odot])$ to the whole population of *GALEX*-selected LBGs, it was found that $a = 5.20 \pm 0.25$ and $b = -0.49 \pm 0.03$ when dust-correcting the rest-frame UV luminosity with the SED-derived $E_s(B - V)$ and $a = 3.95 \pm 0.17$ and $b = -0.38 \pm 0.02$ when dust-correcting the rest-frame UV luminosity with the dust attenuation obtained from the UV continuum slope and the relation of M99. Carrying out the same linear fit to the PACS-detected LBGs studied in this work, we find $a = 10.1 \pm 0.8$ and $b = -0.95 \pm 0.07$. For PACS-detected LBGs, the correlation between the sSFR and the stellar mass has much lower scatter and a higher slope than that for the whole population of LBGs due to the bias produced by the FIR selection. Actually, it can be seen in the right-hand panel of Fig. 17 that, for each stellar mass, PACS only sees the galaxies with the highest sSFRs. However, the sSFR for the most massive galaxies in the sample does not have values as high as the ones derived for the least massive galaxies. This agrees with the downsizing scenario where massive galaxies form their stars earlier and faster than lower massive ones. The absence of massive galaxies with sSFR values as high as those for the least massive ones is not a bias due to the FIR-selection criteria, since massive galaxies with high sSFR

should have been detected with PACS. We do not find any significant difference in the trend between LBGs and UV-faint galaxies in the sSFR–mass diagram: all our PACS-detected galaxies have similar values of the sSFR.

To further analyse the correlation between the sSFR and the stellar mass for IR-fainter LBGs, we also plot in the right-hand plot of Fig. 17 the two points associated with the stacked PACS 160 μm fluxes for the LBGS in the two stellar mass ranges defined in Section 2.2. In agreement with Fig. 8, the values of the sSFR for PACS-detected and PACS-stacked galaxies are within a similar range. The stacked points are deviated from the linear relation found for PACS-detected galaxies towards lower values of the sSFR. This indicates that PACS detections segregate galaxies with the highest sSFR for a given value of stellar mass and that the relation between the sSFR and the stellar mass becomes much wider when introducing IR-faint galaxies.

6 CMD OF THE PACS-DETECTED SOURCES

In this section we study the location of our PACS-detected galaxies in a colour–mCMD. Such a diagram was already studied in Oteo et al. (2013a) for the whole population of LBGs at $z \sim 1$ and it was found that most LBGs occupy the blue cloud of the galaxies at their redshift. Only the dustiest and/or oldest galaxies are distributed over the green valley or the red sequence. In Section 2, we observed that dustier sources are more likely detected in PACS. Therefore, it should be expected that PACS-detected galaxies are located mostly above the blue cloud. This is confirmed in Fig. 18, where LBGs and UV-faint galaxies are represented by red filled dots and green open triangles, respectively. As in Oteo et al. (2013a), the $u - r$ are associated with the magnitudes in the u and r broad-band filters of the Sloan Digital Sky Survey (SDSS). The apparent u and r and absolute r magnitudes are obtained by convolving the best-fitted template of each galaxy with the transmission of the u and r SDSS filters shifted in wavelength according to the redshift of each source.

It can be seen that PACS-detected galaxies are mainly located over the green valley or the red sequence at their redshift. Additionally, there is a difference between LBGs and UV-faint galaxies in the sense that LBGs tend to have bluer optical colours than UV-faint galaxies as a consequence of their lower dust attenuation. UV-faint galaxies are more attenuated by dust and are mostly located near the red sequence despite being actively SF galaxies according to their total SFR.

We also plot in Fig. 18 the location of the PACS-undetected LBGs in order to analyse the difference between PACS-detected and PACS-undetected sources regarding their location in a CMD. Following the same idea as in Oteo et al. (2013a), we divide the sample of PACS-undetected LBGs into *old LBGs*, those whose ages are older than 1200 Myr, and *young LBGs*, those whose ages are younger than 1200 Myr. They are represented by filled and open grey dots, respectively. It can be seen that PACS-detected LBGs are located over a similar zone as old LBGs, which indicates that both old and/or dusty LBGs tend to depart from the blue cloud to the red sequence. This result is similar to that found in Oteo et al. (2013a). It should be noted that here, instead of dividing the sample depending on dust attenuation, we consider PACS-detected and PACS-undetected galaxies separately. Despite this, we still obtain the same result: PACS-detected and/or old LBGs tend to be located over the green valley or the red sequence rather than over the blue cloud. Those LBGs which are located over the blue cloud are only those young and less dusty.
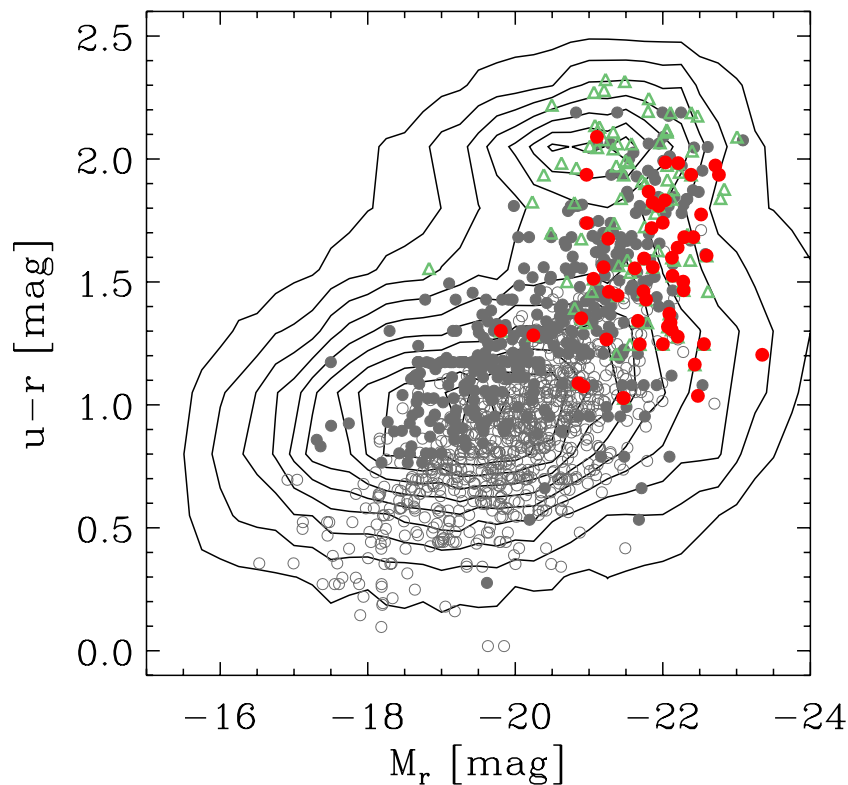
Figure 18. Location of our PACS-detected galaxies in a CMD. The colour $u - r$ is calculated in the rest-frame (see Oteo et al. 2013a). PACS-detected LBGs and UV-selected galaxies are represented with red filled dots and green open triangles, respectively. The grey filled dots represent PACS-undetected LBGs older than 1200 Myr and the grey open dots represent PACS-undetected LBGs younger than 1200 Myr. The black contours represent the CMD of a general sample of galaxies $z \sim 1$ selected from the ALHAMBRA survey.

Therefore, Fig. 18 shows a clear tendency in the CMD as a function of age and dust attenuation, from the less dusty and young galaxies located in the blue cloud to the UV-faint and dusty galaxies located over the red sequence. It also indicates that the properties of LBGs at $z \sim 1$ are diverse. The Lyman break technique seems to select galaxies with different properties but with specific characteristics.

7 MORPHOLOGY OF PACS-DETECTED LBGs

This section is devoted to the study of the morphological properties of our PACS-detected galaxies by carrying out both an analytical and visual procedure. To perform a precise study, high-spatial-resolution ACS images are mandatory. We employ here the publicly available ACS *I*-band images of the COSMOS field. At $z \sim 1$ the ACS *I* band samples the rest-frame *U* band approximately, with little variation according to the redshift distribution of the sources. All our PACS-detected galaxies have available ACS information.

On the visual side, we visually classify the PACS-detected galaxies into five groups, as was done in Oteo et al. (2013a): disc-like galaxies, interacting/merging galaxies, compact galaxies, chain galaxies (CH) or clump clusters (CC), and irregular galaxies. We define disc galaxies as those having a clear disc structure, regardless of the presence of spiral arms or a central bulge. For CH and CC, we employ the definition given in Elmegreen et al. (2009a). Finally, we consider a galaxy as irregular if it cannot be classified within any of the other types. According to a visual classification of their ACS images (see Fig. 19), we obtain that most (68 per cent) PACS-detected LBGs have clear disc-like morphologies. Among them,

59 per cent have flocculent structures (see for example Elmegreen et al. 2009b). For the remaining galaxies, 13 per cent have signs of interaction, 7 per cent are irregular, 7 per cent are CC and 5 per cent belong to the CH class.

On the analytical side, and with the aim of obtaining the physical sizes and examining the radial dependence of the light distribution of the PACS-detected galaxies, we carry out fits to their radial light curves with GALFIT (Peng et al. 2010). In this step, we consider Sérsic profiles (Sersic 1968), which can be described as

$$\Sigma(r) = \Sigma_e \exp \left[-\kappa \left(\left(\frac{r}{R_{\mathrm{eff}}} \right)^{1/n} - 1 \right) \right], \qquad (6)$$

where Σ_e is the pixel surface brightness at the effective radius R_{eff} and n is the concentration parameter or the Sérsic index. The effective radius is the radius which encloses half the light of the galaxy. To make this definition true, the dependent variable κ is coupled to n (Peng et al. 2010). For each input galaxy, GALFIT provides the effective radius (in pixels) and the Sérsic index. In order to convert the effective radius in pixels into the physical size in kpc, we employ the ACS pixel scale and the assumed cosmology for calculating the plate scale at the redshift of each galaxy. The left-hand panel of Fig. 20 represents the distributions of the effective radii of PACS-detected (red shaded histogram) and PACS-undetected LBGs (green histogram). PACS-detected LBGs are large galaxies with effective radii ranging from about 2 to 8 kpc, with a median value of 4 kpc. PACS-undetected LBGs have a median effective radius of $R_{\mathrm{eff}} = 2$ kpc, indicating that FIR detections tend to segregate LBGs with large sizes. There is no significant difference in the physical size between PACS-detected LBGs and PACS-detected UV-selected
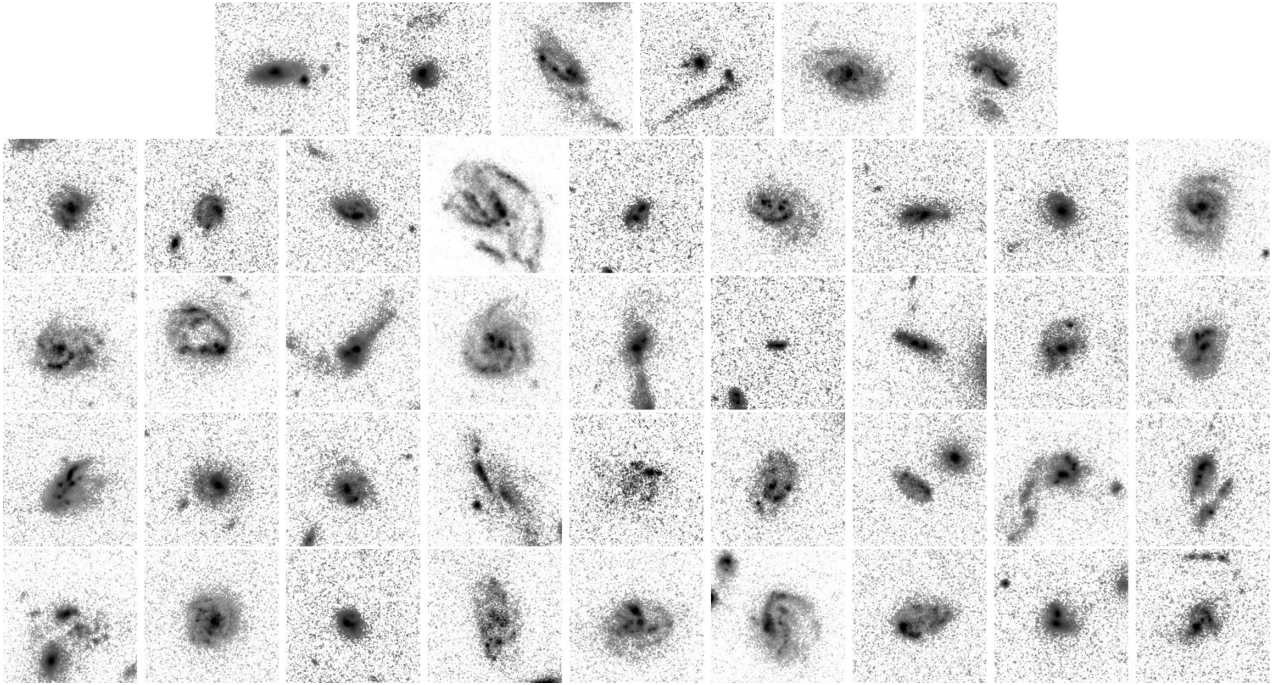
Figure 19. *I*-band optical ACS cutouts of the 42 PACS-detected LBGs. The size of each image is 5 arcsec × 5 arcsec. At $z \sim 1$, the plate scale is 8.008 kpc arcsec^{-1} under the assumed cosmology, and the ACS *I* band samples the rest-frame *U* band approximately.
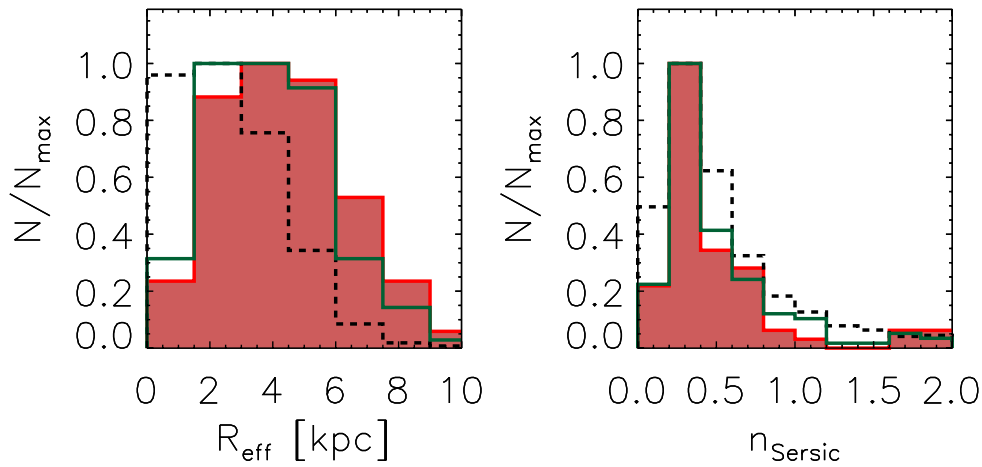

Figure 20. Results of the analytical morphological study of our PACS-detected galaxies. Left: distribution of the physical sizes. Right: distribution of the Sérsic indices. In both panels, PACS-detected LBGs, UV-selected galaxies and PACS-undetected LBGs are represented with red shaded, green and black dashed histograms, respectively. Histograms have been normalized to their maximum in order to clarify the representations.

galaxies. Their Sérsic indices of our PACS-detected LBGs and UV-selected galaxies, shown in the right-hand panel of Fig. 20, vary mostly within $0 \lesssim n \lesssim 0.75$, in agreement with the visual classification that indicates that most PACS-detected LBGs are disc-like galaxies.

8 RADIO MEASUREMENTS

Dust absorbs the UV radiation created from massive stars and re-radiates this light in the IR. When those massive stars explode as SNe, they generate cosmic ray electrons which lose their energy in radio wavelengths, mostly via synchrotron emission. Therefore, it is expected that the radio emission from galaxies is in part related

to their emission in the IR. In this way, radio measurements also provide a powerful tool to obtain SFR.

Following this idea, we analyse in this section the radio emission of the whole sample of LBGs and UV-faint galaxies built in Oteo et al. (2013a) in order to study a possible difference between them and to study the relation between IR- and radio-derived luminosities and SFRs. To this aim, we look for radio counterparts of the whole sample of LBGs and UV-faint galaxies selected in Oteo et al. (2013a) by using data coming from VLA observations of the COSMOS field (Schinnerer et al. 2010). Using again a matching radius of 2 arcsec, we find that 18 LBGs and 46 UV-faint galaxies are detected at 1.4 GHz. These percentages of VLA detections are lower than those corresponding to PACS detections. In order to obtain the rest-frame 1.4 GHz luminosities, since our VLA-detected

yields a probability factor of 0.5, reinforcing the similarity between both distributions.

Obtaining radio-derived SFR requires calculating the IR luminosities associated with the rest-frame 1.4 GHz luminosities by assuming an IR–radio correlation (for example Condon 1992). Then, we first compare in the bottom panel of Fig. 21 the total IR luminosities and the rest-frame 1.4 GHz luminosities for our VLA-detected and PACS-detected galaxies to check if the Condon (1992) relation applies for our galaxies. Nine LBGs and 27 UV-faint galaxies are detected both in PACS and VLA. We also plot there the Condon (1992) IR–radio correlation. It can be seen that PACS-detected UV-faint galaxies are around the Condon (1992) relation and, therefore, for those galaxies, the IR-derived and radio-derived SFRs with the procedure outlined above would agree. PACS-detected LBGs tend to be located slightly above the Condon (1992) relation. This could introduce some differences in the VLA-derived total IR luminosities with respect to those that would be obtained with PACS data. For those PACS-undetected and radio-detected galaxies, we can assume that the Condon (1992) relation is still valid with the aim of calculating the IR luminosity associated with their radio emission. It should be noted that, according to the IR–radio correlation, the SFR_{radio} is a tracer of the SFR_{IR}, but not of the SFR_{total}. Therefore, in order to calculate the total SFR from radio observations, we also have to add the term associated with the UV emission (equation 5). In Fig. 22, we plot the distribution of the total SFR derived from the combination of UV and radio measurements for our VLA-detected galaxies. The median values are 67 ± 65 and $76 \pm 80 \, M_\odot \, yr^{-1}$ for VLA-detected LBGs and UV-faint galaxies, respectively. The uncertainties indicate the standard deviations of the distributions, as a measurement of their width. The total SFRs obtained in Section 4 from the combination of UV and FIR measurements were 91 ± 22 and $73 \pm 39 \, M_\odot \, yr^{-1}$ for PACS-detected LBGs and UV-faint galaxies, respectively. The distributions of radio-derived total SFR are much wider than those obtained from PACS measurements. This is due to the existence of galaxies with very high values of the
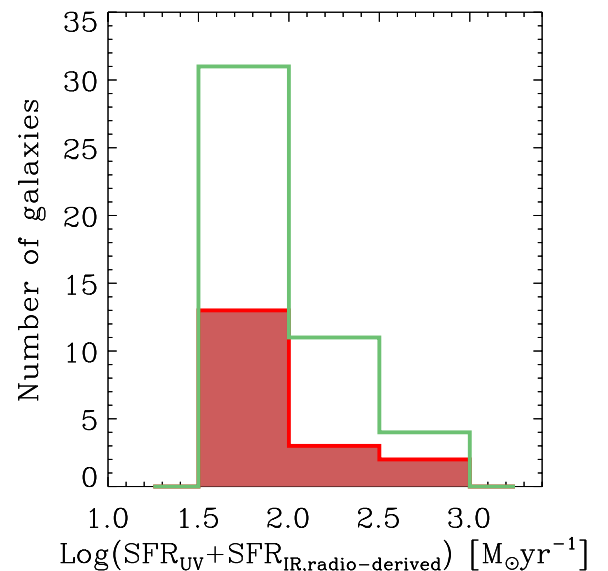

Figure 21. Upper: distribution of the rest-frame 1.4 GHz luminosities for our VLA-detected LBGs (red shaded histogram) and UV-selected galaxies (green histogram). Bottom: relation between the total IR and radio luminosities for our samples of PACS-detected LBGs (red filled dots) and UV-selected galaxies (green open diamonds). The straight line represents the relation of Condon (1992). The blue error bars represent the typical uncertainties of the parameters shown in the *x*- and *y*-axes.

galaxies are located at $z \sim 1$, we must carry out a *K*-correction. To do that, we assume that the radio continuum behaves as $f_{radio} \sim \nu^\alpha$, where α is the radio spectral index, for which we consider a value of $\alpha = -0.8$ (Ivison et al. 2010a,b; Magdis et al. 2010b). We plot in the upper panel of Fig. 21 the distribution of rest-frame 1.4 GHz luminosities for our VLA-detected LBGs and UV-faint galaxies. The low number of detections in radio wavelength of both kinds of galaxies prevents us from distinguishing them according to their radio emission. Actually, both histograms are very similar. A K-S test

Figure 22. Distribution of the total SFR as derived for the combination of UV- and radio-derived IR luminosities for the VLA-detected LBGs (red shaded histogram) and UV-selected galaxies (green histogram). Note that given that we assume that the IR–radio correlation is valid for both IR-detected and IR-undetected sources, in this plot are included all radio detected sources, regardless of the fact that they are detected or not in PACS.
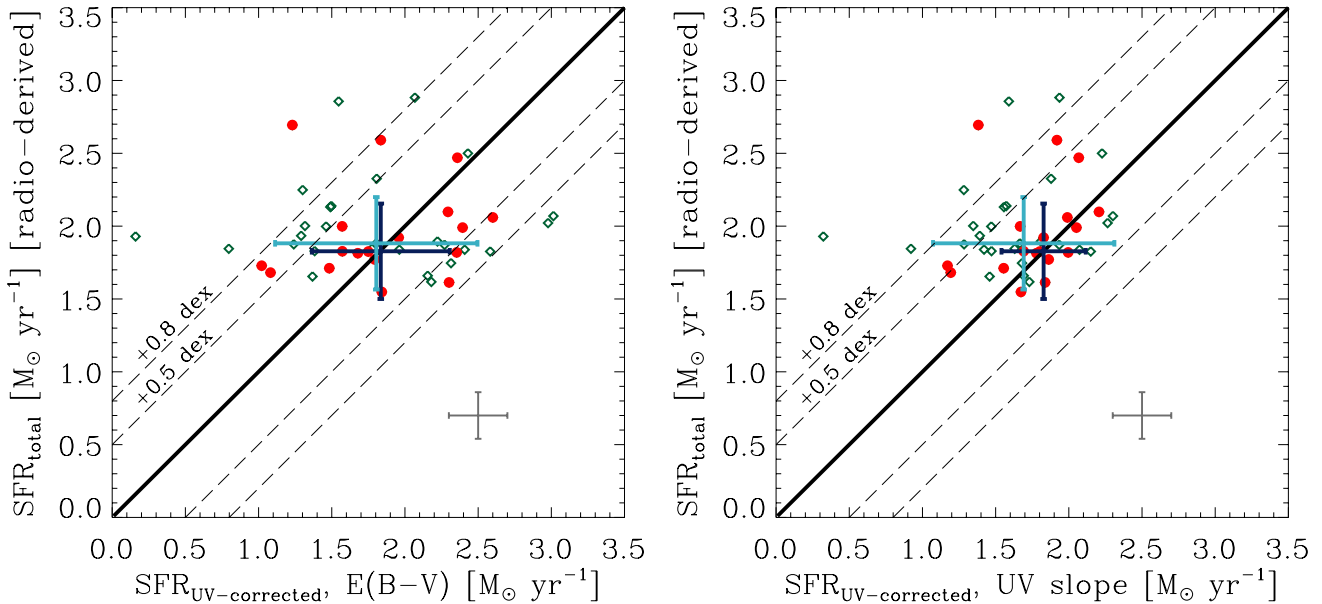
Figure 23. Left: total SFR derived from the combination of UV and radio measurements against the total SFR derived by correcting the rest-frame UV luminosity with the $E_s(B-V)$ value obtained from SED fitting with BC03 templates associated with a constant SFR and sub-solar metallicity $Z = 0.4\,Z_\odot$. Right: total SFR derived from the combination of UV and radio measurements against the total SFR obtained by correcting the rest-frame UV luminosity with the UV continuum slope and applying the M99 relation. In both panels, VLA-detected LBGs and UV-selected galaxies are represented with red open dots and green open diamonds, respectively. The median loci in the diagrams of the PACS-detected LBGs and UV-selected galaxies are represented by the dark blue and light blue bars, respectively. The bars cross in the median value of each parameter for each kind of galaxy and the length of the bars is the standard deviation of the distribution of values. The lines represent where both estimators would agree. The grey error bars represent the typical uncertainties of the parameters shown in the *x*- and *y*-axes.

radio-derived total SFR compared to the median of the distributions. Despite this, there is very good agreement between the radio and FIR determinations.

Finally, we study in Fig. 23 the relation between the SED-derived dust-corrected total SFR and the total SFR derived from the combination of UV and radio measurements. These are similar plots as those presented in Figs 14 and 15. As in that case, we use the dust-corrected SED-derived total SFRs obtained from the best-fitted $E_s(B-V)$ value and from the dust attenuation obtained with the UV continuum slope by applying the M99 relation. It can be seen that both procedures tend to give similar results, providing estimation of the total SFR within 0.8 dex for most of the galaxies. Furthermore, this spread around the one-to-one relation is similar to that found in Figs 14 and 15 when using PACS data to obtain the UV+IR-derived total SFR.

9 CONCLUSIONS

In this work, they have analysed the UV-to-FIR SED of a sample of LBGs and other UV-selected galaxies at $z \sim 1$ located in the COS-MOS field. To this aim, we have used data coming from *GALEX*, ALHAMBRA survey, IRAC, MIPS and PACS 100 μm/160 μm observations. The combination of all these measurements provides an unprecedented coverage of the SED of galaxies at the studied redshift. The sample of LBGs was selected via their FUV − NUV colour. Due to their selection criteria, LBGs are UV-bright galaxies. For comparison, we also retain a sample of UV-selected and PACS-detected galaxies fainter in the UV than LBGs but located at the same redshift range. We call these sources *UV-faint galaxies*. The main conclusions of the work can be summarized as follows.

(i) We have found that, among a sample of 1225 UV-selected LBGs at $z \sim 1$, 42 of them are individually detected in either

PACS 100 μm or PACS 160 μm under depths of 5.0 and 11.0 mJy in each band, respectively. These measurements, in combination with ancillary IRAC 8.0 μm and MIPS 24 μm data, provide a good sampling of the mid-IR/FIR SED of these galaxies. This allows an accurate determination of their total IR luminosity, dust attenuation, and total and sSFR. PACS-detected LBGs tend to have higher rest-frame UV luminosities, dust attenuation and stellar mass, and have redder UV continuum than PACS-undetected galaxies. There is no relation in age between PACS-detected and PACS-undetected LBGs.

(ii) All PACS-detected LBGs have total IR luminosities $10^{11} \lesssim L_{IR}/L_\odot \lesssim 10^{12}$ and, therefore, are all LIRGs. The lower limit range of total IR luminosities is a direct consequence of the depth of the PACS observations employed in this work. However, there are no PACS-detected LBGs in the ULIRG regime, $L_{IR}/L_\odot \geq 10^{12}$, where the observations are complete. At $z \sim 3$, the PACS-detected LBGs found so far are all ULIRGs. This suggests that the FIR emission of galaxy is changing with cosmic time in the sense that at higher redshifts, there is a population of extreme IR-bright, red and dusty LBGs which is not found at intermediate redshifts.

(iii) By using their UV and IR emissions and applying the Buat et al. (2005) calibration, we find that PACS-detected LBGs have dust attenuation spanning $2 \lesssim A_{1200\,\text{Å}}[\text{mag}] \lesssim 5$, with a median value of 4 mag. PACS-detected LBGs, due to their brightness in the UV as a consequence of their selection criteria, are less dusty than other UV-fainter galaxies at the same redshift. PACS-detected LBGs with higher rest-frame UV luminosities are less attenuated. Furthermore, the dust attenuation of PACS-detected LBGs increases with the total IR luminosity.

(iv) According to the combination of their UV and IR emission, PACS-detected LBGs have a median total SFR of 90 $M_\odot$ yr^{-1}. The SED-derived dust attenuation obtained with BC03 templates

associated with a constant SFR tends to overestimate the total SFR obtained from the combination of UV and IR measurements for the youngest galaxies in the sample. This is likely due to the typical degeneracy between age and dust attenuation in the SED-fitting procedures with synthetic templates and highlights the importance of the usage of direct UV and IR measurements when obtaining the total SFR and dust attenuation in galaxies.

(v) The dust attenuation derived from rest-frame UV to NIR SED fitting overestimates the total SFR for most of our PACS-detected LBGs in an age-dependent way: the overestimation factor is higher for younger galaxies. This is likely due to the degeneracy in the SED-fitting procedures between dust attenuation, age and SFH, and highlights the importance of using direct FIR detections of galaxies to obtain accurate values of their IR luminosities, dust attenuation and total SFR.

(vi) By analysing the location of our PACS-detected LBGs in an IRX–β diagram, we find that they are mostly around the M99 relation for local SB, but above the corrections of T12 and O11 to the M99 law. This is also true for other UV-selected PACS-detected galaxies. Consequently, the dust-correction factors obtained with the M99 relation can be used to recover the dust attenuation of our PACS-detected galaxies. This does not have to be true for other less dusty and PACS-undetected galaxies, since PACS only detects the dustiest and IR-brightest galaxies at $z \sim 1$.

(vii) In a CMD diagram, PACS-detected LBGs have red optical colour compatible with them being mostly located over the green valley or the red sequence despite being active SF galaxies. UV-faint galaxies are also located over the green valley and the red sequence, although there is a larger percentage of galaxies populating the red sequence than in the sample of PACS-detected LBGs. PACS-undetected LBGs with ages larger than 1200 Myr tend to be also located over the green valley and the red sequence. This indicates that the properties of LBGs at $z \sim 1$ are diverse, from blue, young, PACS-undetected LBGs to old or PACS-detected red LBGs.

(viii) Morphologically, ACS *I*-band (sampling the rest-frame *U* band at $z \sim 1$) imaging indicates that 68 per cent PACS-detected LBGs are disc-like galaxies, with 59 per cent of them having flocculent structures, and 13 per cent have signs of interactions. There is a low percentage (<7 per cent) of irregular, CH or CC galaxies. The median effective radius of the PACS-detected LBGs is 4 kpc. This value is higher than that for PACS-undetected LBGs, $R_{\rm eff} = 2$ kpc, indicating that FIR detections tend to segregate galaxies with larger sizes. The Sérsic indices of PACS-detected are compatible with them being disc galaxies.

(ix) The radio measurements of our galaxies also provide accurate determinations of their total SFR. The IR/UV- and radio/UV-derived total SFRs are in agreement due to the validity of the Condon (1992) relation for most of our galaxies at $z \sim 1$. The dust correction obtained from the UV continuum slope and the application of the M99 relation gives much better results for the total SFR than the dust correction carried out with the SED-derived $E_s(B - V)$.

ACKNOWLEDGEMENTS

REFERENCES

Atek H. et al., 2011, ApJ, 743, 121
Barger A. J., Cowie L. L., Wang W.-H., 2008, ApJ, 689, 687
Basu-Zych A. R., Hornschemeier A. E., Hoversten E. A., Lehmer B., Gronwall C., 2011, ApJ, 739, 98
Boissier S. et al., 2007, ApJS, 173, 524 (B07)
Boquien M. et al., 2009, ApJ, 706, 553
Boquien M. et al., 2012, A&A, 539, A145

Bouwens R. J., Illingworth G. D., Blakeslee J. P., Franx M., 2006, ApJ, 653, 53

Bouwens R. J. et al., 2009, ApJ, 705, 936

Bouwens R. J. et al., 2012, ApJ, 754, 83

Bruzual G., Charlot S., 2003, MNRAS, 344, 1000 (BC03)

Buat V. et al., 2005, ApJ, 619, L51

Buat V., Takeuchi T. T., Burgarella D., Giovannoli E., Murata K. L., 2009, A&A, 507, 693

Buat V. et al., 2010, MNRAS, 409, L1

Buat V. et al., 2012, A&A, 545, A141

Burgarella D. et al., 2006, A&A, 450, 69

Burgarella D., Le Floc'h E., Takeuchi T. T., Huang J. S., Buat V., Rieke G. H., Tyler K. D., 2007, MNRAS, 380, 986

Burgarella D. et al., 2011, ApJ, 734, L12

Calzetti D., Kinney A. L., Storchi-Bergmann T., 1994, ApJ, 429, 582

Calzetti D., Armus L., Bohlin R. C., Kinney A. L., Koornneef J., Storchi-Bergmann T., 2000, ApJ, 533, 682

Capak P. et al., 2007, ApJS, 172, 99

Castellano M. et al., 2012, A&A, 540, A39

Chapman S. C., Casey C. M., 2009, MNRAS, 398, 1615

Chapman S. C. et al., 2000, MNRAS, 319, 318

Chary R., Elbaz D., 2001, ApJ, 556, 562 (CE01)

Chen Z., Shu C. G., Burgarella D., Buat V., Huang J.-S., Luo Z. J., 2013, MNRAS, 431, 2080

Condon J. J., 1992, ARA&A, 30, 575

Daddi E. et al., 2007, ApJ, 670, 156

Dale D. A., Helou G., 2002, ApJ, 576, 159 (DH02)

Damen M., Förster Schreiber N. M., Franx M., Labbé I., Toft S., van Dokkum P. G., Wuyts S., 2009, ApJ, 705, 617

Davies L. J. M., Bremer M. N., Stanway E. R., Lehnert M. D., 2013, MNRAS, 433, 2588

de Barros S., Schaerer D., Stark D. P., 2012, arXiv:e-prints

Diolaiti E., Bendinelli O., Bonaccini D., Close L., Currie D., Parmeggiani G., 2000a, A&AS, 147, 335

Diolaiti E., Bendinelli O., Bonaccini D., Close L. M., Currie D. G., Parmeggiani G., 2000b, Proc. SPIE, 4007, 879

Dunlop J. S., McLure R. J., Robertson B. E., Ellis R. S., Stark D. P., Cirasuolo M., de Ravel L., 2012, MNRAS, 420, 901

Dunne L. et al., 2009, MNRAS, 394, 3

Elbaz D. et al., 2007, A&A, 468, 33

Elbaz D. et al., 2010, A&A, 518, L29

Elbaz D. et al., 2011, A&A, 533, A119

Elmegreen B. G., Elmegreen D. M., Fernandez M. X., Lemonias J. J., 2009a, ApJ, 692, 12

Elmegreen D. M., Elmegreen B. G., Marcus M. T., Shahinyan K., Yau A., Petersen M., 2009b, ApJ, 701, 306

Elvis M. et al., 2009, ApJS, 184, 158

Erb D. K., Steidel C. C., Shapley A. E., Pettini M., Reddy N. A., Adelberger K. L., 2006, ApJ, 647, 128

Feldmann R. et al., 2006, MNRAS, 372, 565

Feulner G., Goranova Y., Drory N., Hopp U., Bender R., 2005a, MNRAS, 358, L1

Feulner G., Gabasch A., Salvato M., Drory N., Hopp U., Bender R., 2005b, ApJ, 633, L9

Finkelstein S. L., Malhotra S., Rhoads J. E., Hathi N. P., Pirzkal N., 2009, MNRAS, 393, 1174

Finkelstein S. L. et al., 2012, ApJ, 756, 164

Giovannoli E., Buat V., Noll S., Burgarella D., Magnelli B., 2011, A&A, 525, A150

Goldader J. D., Meurer G., Heckman T. M., Seibert M., Sanders D. B., Calzetti D., Steidel C. C., 2002, ApJ, 568, 651

González V., Labbé I., Bouwens R. J., Illingworth G., Franx M., Kriek M., Brammer G. B., 2010, ApJ, 713, 115

González V., Labbé I., Bouwens R. J., Illingworth G., Franx M., Kriek M., 2011, ApJ, 735, L34

Griffin M. J. et al., 2010, A&A, 518, L3

Haberzettl L., Williger G., Lehnert M. D., Nesvadba N., Davies L., 2012, ApJ, 745, 96

Hathi N. P., Malhotra S., Rhoads J. E., 2008, ApJ, 673, 686

Hathi N. P. et al., 2010, ApJ, 720, 1708

Hathi N. P. et al., 2013, ApJ, 765, 88

Heinis S. et al., 2013, MNRAS, 429, 1113

Ivison R. J. et al., 2010a, MNRAS, 402, 245

Ivison R. J. et al., 2010b, A&A, 518, L31

Iwata I., Ohta K., Tamura N., Akiyama M., Aoki K., Ando M., Kiuchi G., Sawicki M., 2007, MNRAS, 376, 1557

Karim A. et al., 2011, ApJ, 730, 61

Kennicutt R. C., Jr, 1998, ARA&A, 36, 189

Kong X., Charlot S., Brinchmann J., Fall S. M., 2004, MNRAS, 349, 769

Le Floc'h E. et al., 2009, ApJ, 703, 222

Lee K.-S., Alberts S., Atlee D., Dey A., Pope A., Jannuzi B. T., Reddy N., Brown M. J. I., 2012, ApJ, 758, L31

Lilly S. J. et al., 2007, ApJS, 172, 70

Lutz D. et al., 2011, A&A, 532, A90

Ly C. et al., 2009, ApJ, 697, 1410

Ly C., Malkan M. A., Hayashi M., Motohara K., Kashikawa N., Shimasaku K., Nagao T., Grady C., 2011, ApJ, 735, 91

Madau P., 1995, ApJ, 441, 18

Madau P., Ferguson H. C., Dickinson M. E., Giavalisco M., Steidel C. C., Fruchter A., 1996, MNRAS, 283, 1388

Magdis G. E., Rigopoulou D., Huang J.-S., Fazio G. G., 2010a, MNRAS, 401, 1521

Magdis G. E., Elbaz D., Daddi E., Morrison G. E., Dickinson M., Rigopoulou D., Gobat R., Hwang H. S., 2010b, ApJ, 714, 1740

Magdis G. E. et al., 2010c, ApJ, 720, L185

Magnelli B., Elbaz D., Chary R. R., Dickinson M., Le Borgne D., Frayer D. T., Willmer C. N. A., 2009, A&A, 496, 57

Meurer G. R., Heckman T. M., Calzetti D., 1999, ApJ, 521, 64 (M99)

Moles M. et al., 2008, AJ, 136, 1325

Murphy E. J., Chary R.-R., Dickinson M., Pope A., Frayer D. T., Lin L., 2011, ApJ, 732, 126

Noeske K. G. et al., 2007, ApJ, 660, L43

Nordon R. et al., 2013, ApJ, 762, 125

Oke J. B., Gunn J. E., 1983, ApJ, 266, 713

Oliver S. J. et al., 2010, A&A, 518, L21

Oteo I. et al., 2011, ApJ, 735, L15

Oteo I. et al., 2012a, A&A, 541, A65

Oteo I. et al., 2012b, ApJ, 751, 139

Oteo I. et al., 2013a, MNRAS, submitted

Oteo I. et al., 2013b, A&A, 554, L3

Overzier R. A. et al., 2011, ApJ, 726, L7 (O11)

Pannella M. et al., 2009, ApJ, 698, L116

Peng C. Y., Ho L. C., Impey C. D., Rix H., 2010, AJ, 139, 2097

Pilbratt G. L. et al., 2010, A&A, 518, L1

Poglitsch A. et al., 2010, A&A, 518, L2

Reddy N. A., Steidel C. C., Fadda D., Yan L., Pettini M., Shapley A. E., Erb D. K., Adelberger K. L., 2006, ApJ, 644, 792

Reddy N. A., Erb D. K., Pettini M., Steidel C. C., Shapley A. E., 2010, ApJ, 712, 1070

Reddy N. et al., 2012, ApJ, 744, 154

Rigopoulou D. et al., 2010, MNRAS, 409, L7

Rodighiero G. et al., 2010, A&A, 518, L25

Salim S. et al., 2007, ApJS, 173, 267

Salmi F., Daddi E., Elbaz D., Sargent M. T., Dickinson M., Renzini A., Bethermin M., Le Borgne D., 2012, ApJ, 754, L14

Salpeter E. E., 1955, ApJ, 121, 161

Salvato M. et al., 2011, ApJ, 742, 61

Sanders D. B. et al., 2007, ApJS, 172, 86

Sawicki M., 2012, MNRAS, 421, 2187

Schaerer D., de Barros S., 2009, A&A, 502, 423

Schaerer D., de Barros S., 2010, A&A, 515, A73

Schaerer D., de Barros S., Stark D. P., 2011, A&A, 536, A72

Schaerer D., de Barros S., Sklias P., 2013, A&A, 549, A4

Schinnerer E. et al., 2010, ApJS, 188, 384

Scoville N. et al., 2007, ApJS, 172, 1

Sérsic J. L., 1968, in Sérsic J. L., ed., Atlas de galaxias australes. Observatorio Astronomico, Cordoba, Argentina

Siana B. et al., 2009, ApJ, 698, 1273

Stark D. P., Schenker M. A., Ellis R., Robertson B., McLure R., Dunlop J., 2013, ApJ, 763, 129

Steidel C. C., Giavalisco M., Dickinson M., Adelberger K. L., 1996, AJ, 112, 352

Steidel C. C., Adelberger K. L., Giavalisco M., Dickinson M., Pettini M., 1999, ApJ, 519, 1

Steidel C. C., Adelberger K. L., Shapley A. E., Pettini M., Dickinson M., Giavalisco M., 2003, ApJ, 592, 728

Takeuchi T. T., Buat V., Heinis S., Giovannoli E., Yuan F.-T., Iglesias-Páramo J., Murata K. L., Burgarella D., 2010, A&A, 514, A4

Takeuchi T. T., Yuan F.-T., Ikeyama A., Murata K. L., Inoue A. K., 2012, ApJ, 755, 144 (T12)

Verma A., Lehnert M. D., Förster Schreiber N. M., Bremer M. N., Douglas L., 2007, MNRAS, 377, 1024

Vijh U. P., Witt A. N., Gordon K. D., 2003, ApJ, 587, 533

Wilkins S. M., Bunker A. J., Stanway E., Lorenzoni S., Caruana J., 2011, MNRAS, 417, 717

Wilkins S. M., Gonzalez-Perez V., Lacey C. G., Baugh C. M., 2012, MNRAS, 424, 1522

Yabe K., Ohta K., Iwata I., Sawicki M., Tamura N., Akiyama M., Aoki K., 2009, ApJ, 693, 507

Zackrisson E., Bergvall N., Leitet E., 2008, ApJ, 676, L9

APPENDIX A: DEPENDENCE OF THE RESULTS ON THE ASSUMED SFH

Throughout this work, we have used a set of BC03 templates which were built by using an SFH constant with time. In the elaboration of the BC03 templates, other temporal functions can be assumed for the SFH associated with the templates. One of the most used temporal variation is that when the SFH is exponentially declining with time. In this case, the SFH is characterized by the time-scale, τ_{SFH}. This is an extra parameter to fit in the SED-fitting procedure in addition to age and dust attenuation (assuming that we only consider one value of metallicity). Three questions arise now: Do the SED-fitting-derived values of age and dust attenuation for our PACS-detected galaxies change with the assumed SFH? Once we assume an exponentially declining SFH, do the SED-fitting-derived values of age and dust attenuation for our PACS-detected galaxies change with different assumed values of the time-scale τ_{SFH}? Finally, and most important, in the case that there is a dependence of age and dust attenuation on τ_{SFH}, can an SED fitting with BC03 templates to the observed UV-to-near-IR photometry distinguish which is the right value of the star formation time-scale and, therefore, give the right values of age and dust attenuation?
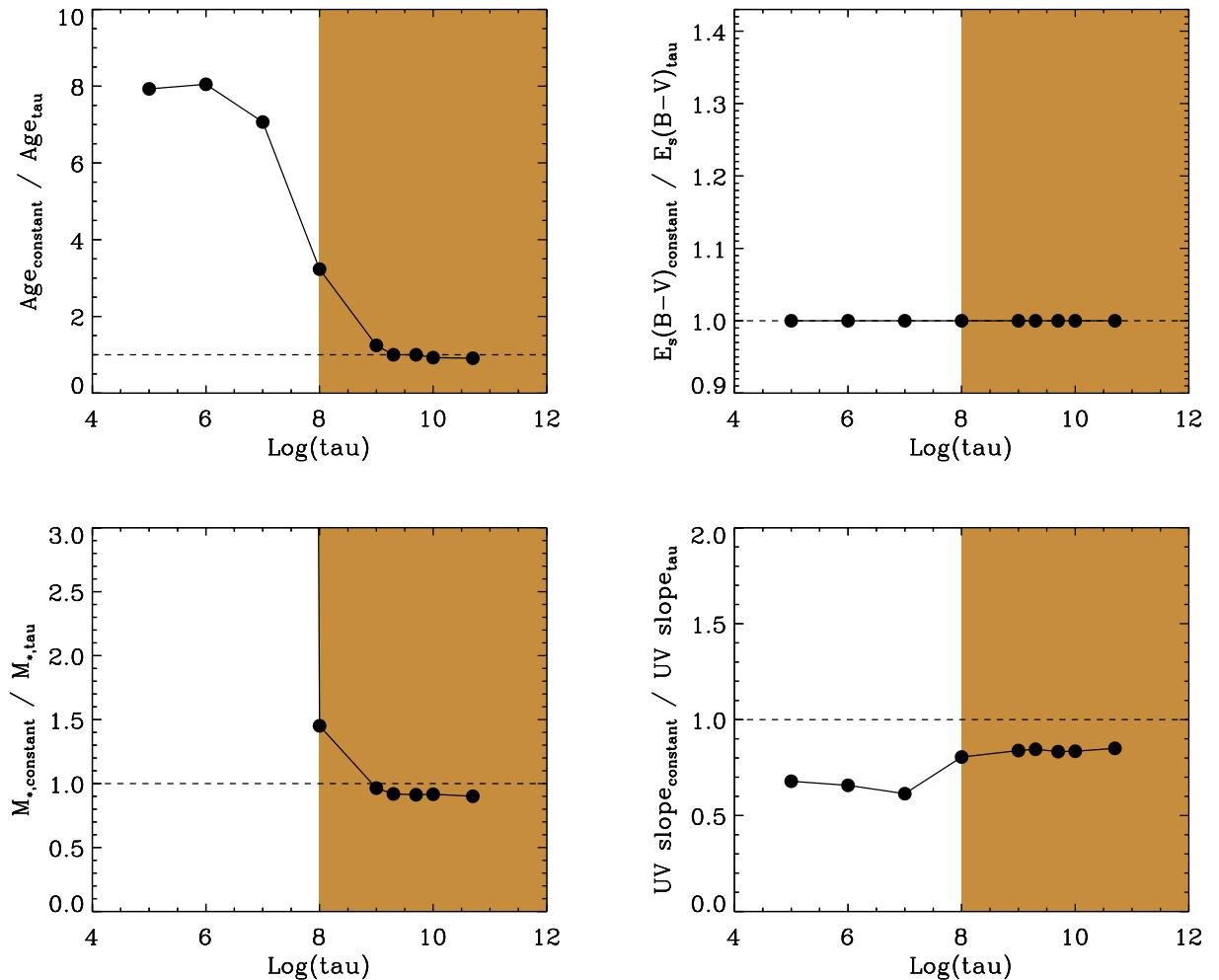

Figure A1. Ratios between the SED-derived age (upper left), dust attenuation (upper right), stellar mass (bottom left) and UV continuum slope (bottom right) when assuming a constant SFH and SFHs associated with different values of the time-scale. In this plot, all our PACS-detected sources are included as a whole sample of UV-selected FIR-detected galaxies at $z \sim 1$. These ratios are represented as a function of the logarithm of the star formation time-scale expressed in Gyr. The horizontal dashed lines represent where the SED-derived values associated with different SFHs would agree. The shaded zones are those corresponding to realistic values of the star formation time-scale for our PACS-detected galaxies at $z \sim 1$.
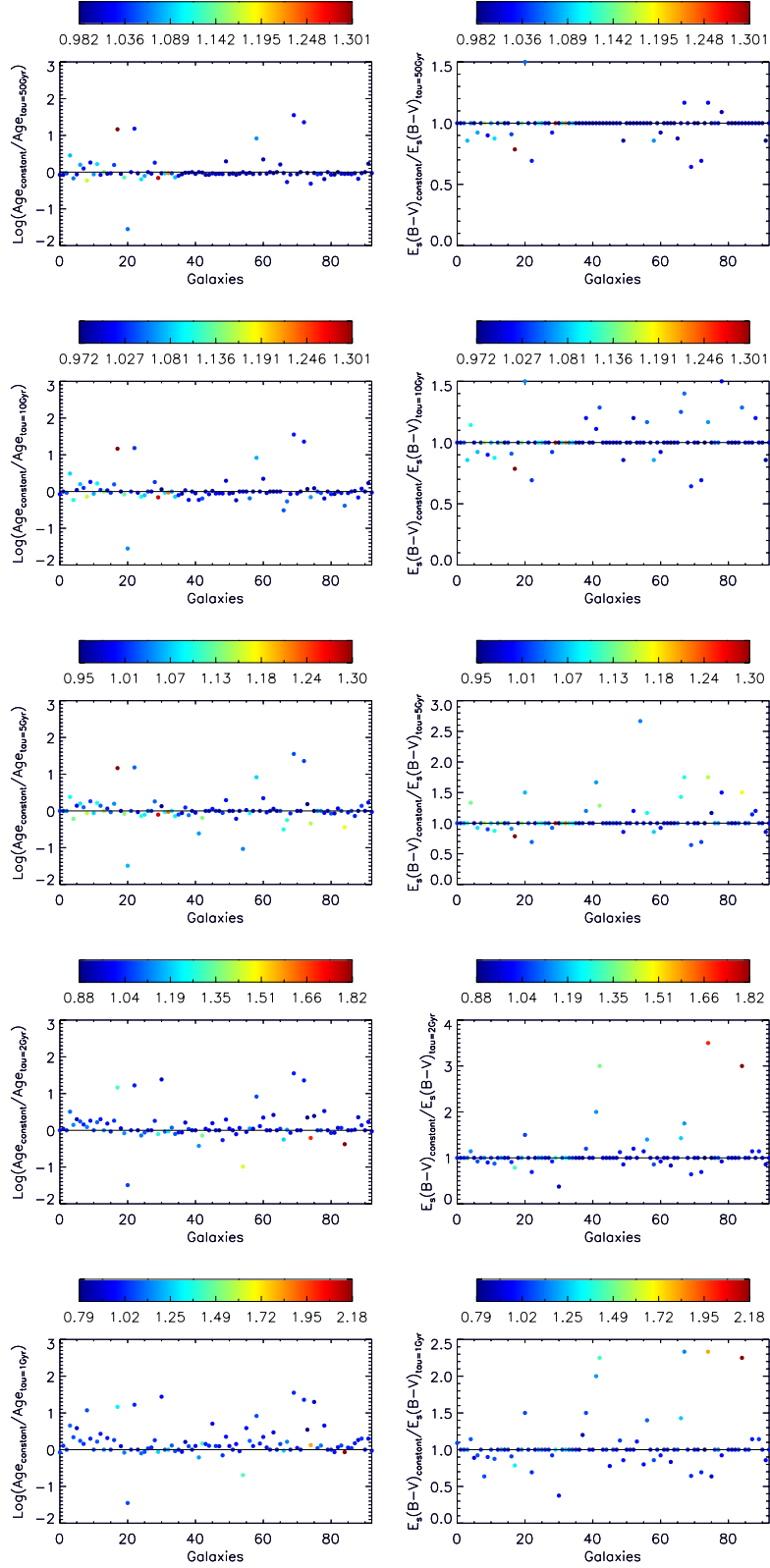
Figure A2. Left column: relation between the ages derived with an SED-fitting procedure when considering a constant SFH and an exponentially declining SFH for different values of the SFH time-scale. Right column: relation between the dust attenuation derived with an SED-fitting procedure when considering a constant SFH and an exponentially declining SFH for different values of the SFH time-scale. Each point in the plots represents one PACS-detected galaxy. Each row is related to a specific value of the star formation time-scale, τ_{SFH}, as indicated in each vertical axis. The SFR time-scales considered are $\tau_{SFH} = 50$, 10, 5, 2 and 1 Gyr in the first, second, third, fourth and sixth rows, respectively. The colour of each point is related to the ratio of the χ^2 values between the SED fittings carried out by considering a constant and an exponentially declining SFH: $\chi^2_{constant}/\chi^2_{\tau_{SFH}}$. The colour code for the values of $\chi^2_{constant}/\chi^2_{\tau_{SFH}}$ is indicated in the colour bars. In all the plots, the horizontal line represents where both quantities represented in each vertical axis would agree.
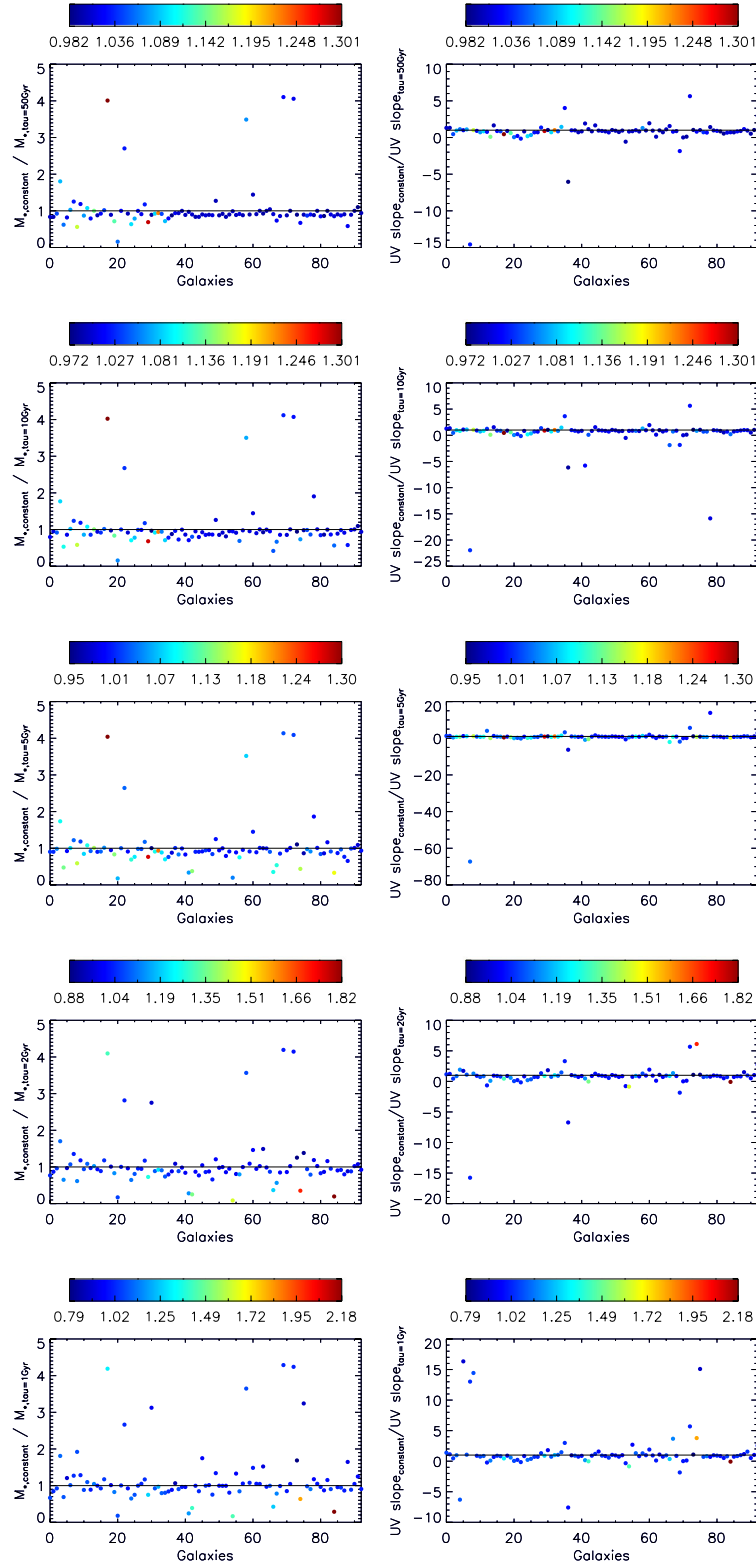
Figure A3. Left column: relation between the stellar mass derived with an SED-fitting procedure when considering a constant SFH and an exponentially declining SFH for different values of the SFH time-scale. Right column: relation between the UV continuum slope derived with an SED-fitting procedure when considering a constant SFH and an exponentially declining SFH for different values of the SFH time-scale. Each point in the plots represents one PACS-detected galaxy. Each row is related to a specific value of the star formation time-scale, τ_{SFH}, as indicated in each vertical axis. The SFR time-scales considered are $\tau_{\mathrm{SFH}} = 50, 10, 5, 2$ and 1 Gyr in the first, second, third, fourth and sixth rows, respectively. The colour of each point is related to the ratio of the χ^2 values between the SED fittings carried out by considering a constant and an exponentially declining SFH: $\chi^2_{\mathrm{constant}}/\chi^2_{\tau_{\mathrm{SFH}}}$. The colour code for the values of $\chi^2_{\mathrm{constant}}/\chi^2_{\tau_{\mathrm{SFH}}}$ is indicated in the colour bars. In all the plots, the horizontal line represents where both quantities represented in each vertical axis would agree.

In this appendix, we analyse the possible differences in the SED-derived parameters when using different temporal dependences of the SFH with different values of the time-scale τ_{SFH}. To this aim, we build another set of BC03 templates assuming time-declining SFHs with values of the time-scale $\tau_{SFH} = [0.0001, 0.001, 0.01, 0.1, 1.0, 2.0, 5.0, 10.0, 50.0]$ Gyr. It should be noted that a constant SFH is an exponentially declining SFH when the star formation time-scale tends to infinity.

In order to analyse if the SED-fitting-derived results depend on the assumed SFH, we show in Fig. A1 the relation between the SED-derived age, dust attenuation, stellar mass and UV continuum slope for our PACS-detected galaxies when assuming a constant SFH and temporal exponentially declining SFHs associated with different star formation time-scales. Each point in the plots represents the median value for all the PACS-detected galaxies. It can be seen that age and stellar mass are the most dependent parameters on the assumption of the SFH. Both parameters are lower with respect to the value associated with a constant SFR when τ_{SFH} decreases. The median values of the dust attenuation do not strongly depend on the assumed SFR and regarding the UV continuum slope, it tends to change to lower values when the τ_{SFR} is low. In this analysis, we have considered a wide range of values for the star formation time-scale in order to give a general vision of what happens to the SED-fitting results when the SFH is modified. However, among the values considered, only those $\tau_{SFH} > 0.1$ could be considered as realistic cases for our galaxies at the studied redshifts. Lower values of the star formation time-scale would lead to a passively evolving galaxy in which an instant burst took place in the onset of the star formation. This is not probably the most realistic picture for UV-selected FIR-detected galaxies, which are actively SF galaxies according to their selection in the rest-frame UV and their detection in the FIR. The regions associated with realistic values for our PACS-detected galaxies are those shaded in Fig. A1. It can be seen that considering only star formation time-scales in the realistic zone, the SED-derived ages when considering a declining SFH are lower than those in the constant SFR case by a maximum factor of about 3. Dust attenuation is the same in all the cases. The SED-derived stellar masses are slightly higher when considering a declining SFH for values of the star formation time-scales higher than about 1 Gyr, and are higher by a maximum factor of 1.5 for $\tau_{SFH} < 1$ Gyr. Regarding the UV continuum slopes, they are lower in the case of a declining SFH in a maximum factor of 0.8.

We have just seen that the SED-fitting-derived physical properties of our galaxies slightly change with the assumption of the SFH. Now we address the question if we can distinguish between different kinds of SFH with an SED-fitting procedure with the good photometric coverage that the combination of *GALEX* and ALHAMBRA provides. To this aim, we have to study if the χ^2 of the SED fits change significantly with the assumed SFH. If the χ^2 value associated with an SED fit obtained, for example, with a constant SFH is much lower than the χ^2 associated with any other SED fit obtained with an exponentially decaying SFH, we could ensure that the right

SFH is that constant with time and, therefore, establish that the age, dust attenuation, stellar mass and UV continuum slope are those associated with the template of constant SFH. In Figs A2 and A3, we present the ratio between the SED-derived age, dust attenuation, stellar mass and UV continuum slope when considering BC03 templates associated with a constant SFR and exponentially decaying SFHs. This ratio is represented as a function of an ID number which represents each PACS-detected galaxy. The colour of each point is related to $\chi^2_{constant}/\chi^2_{\tau_{SFH}}$, the ratio of χ^2 values of the SED fits carried out with BC03 templates associated with a constant and an exponentially declining SFH, respectively. Each plot in Fig. A2 is linked to a specific value of the star formation time-scale. It can be seen that the $\chi^2_{constant}/\chi^2_{\tau_{SFH}}$ ratios are close to unity for most of the galaxies and for most values of τ_{SFH}. Therefore, we conclude that by employing SED fittings with BC03 templates we cannot distinguish between different types of SFHs and, therefore, we have a lack of knowledge of the specific SFH of each galaxy. Combining this result to the fact that different values of the assumed star formation time-scale tend to give different values of some SED-derived physical properties, we conclude that even when using the exceptional photometric coverage that the combination of *GALEX* and ALHAMBRA data provides, we cannot obtain completely accurate values of the SED-derived properties of our PACS-detected galaxies. For example, in the case of the SED-derived age, as it tends to decrease with respect to the constant SFR case when the star formation time-scale decreases, the derived values of the age derived with BC03 templates associated with a constant SFR could be considered as an upper limit of the real age of the galaxy. In this way, if we obtain that a galaxy is young, it would also be young when considering other kinds of SFHs.

We wonder now what are the implications of the degeneration of the assumed SFH on the figures analysed in this work. It only affects to the analysis involving the age, stellar mass and the UV continuum slope since, as we have just seen, the SED-derived dust attenuation does not strongly change with the assumed SFH. Therefore, we have to pay special attention to the location of the galaxies in the star formation versus stellar mass diagram (Fig. 17) and in the IRX–β diagram (Fig. 11). As commented in Section 5, the total SFRs shown in the vertical axis are derived from the combination of UV and IR emission, whereas the stellar masses are those SED derived. Therefore, the *x*-axis values are those depending on the assumed SFH. Since the stellar mass derived with BC03 templates associated with an exponentially decaying SFH is higher with respect to the value associated with a constant SFR, it is expected that we would have obtained that the galaxies are closer to the MS. In any case, the differences found in the SED-derived parameters when assuming different SFH scenarios are within their typical uncertainties and, therefore, the choice of a fixed SFH does not strongly affect our results.

This paper has been typeset from a TEX/LATEX file prepared by the author.